Bioactive Materials 48 (2025) 531–549

Contents lists available at ScienceDirect

Bioactive Materials

journal homepage: www.keaipublishing.com/en/journals/bioactive-materials

# Topological cues of microparticles train stem cells for tissue repair via mechanotransduction

Jiannan Mao [a,b,1], Yichang Xu [a,1], Wenbo Wang [a,1], Xiongwei Deng [b,1], Yujian Hui [a,b], Min Rui [a,b], Jincheng Tang [a], Wei Wang [a], Yiyang Huang [a], Liang Wu [c], Kun Xi [a,*], Yunrong Zhu [b,**], Yong Gu [a,***], Liang Chen [a,****]

[a] Department of Orthopedics, The First Affiliated Hospital of Soochow University, Orthopedic Institute, Soochow University, 188 Shizi Road, Suzhou, Jiangsu, 215006, PR China

[b] Department of Orthopaedics, Wuxi Key Laboratory of Biomaterials for Clinical Application, Department of Central Laboratory, Jiangyin Clinical College of Xuzhou Medical University, No.163 Shoushan Road, Jiang Yin, 214400, PR China

[c] Division of Spine Surgery, Department of Orthopedic Surgery, Nanjing Drum Tower Hospital, Affiliated Hospital of Medical School, Nanjing University, Nanjing, 210008, PR China

ARTICLE INFO

*Keywords:*
Bone regeneration
Topological cues
Microparticle
Focal adhesion
YAP
Mechanotransduction

ABSTRACT

Microspheres (MPs) and porous microspheres (PMPs) are the two most widely used microparticles in tissue engineering and stem cell therapy. However, how stem cells perceive the topological differences between them to regulate cell function remains to be unclear. Here, we systematically studied the changes in stem cell function under the action of MPs and PMPs and elucidated the related mechanisms. Our findings show that the porous structure of PMPs can be sensed by focal adhesions (FAs), which triggers the synthesis of F-actin to inhibit the phosphorylation and degradation of Yes-associated protein (YAP), while also transmitting stress to the nucleus through the contraction of F-actin, thereby enhancing the nuclear translocation of YAP protein. The activation of YAP significantly enhances the proliferation, osteogenesis, paracrine and glucose metabolism of BMSCs, making them exhibit stronger bone repair ability in both in vivo and in vitro experiments. In summary, this study provides a comprehensive and reliable understanding of the behavior of BMSCs in response to MPs and PMPs. It also deepens our understanding of the association between microparticles' topological cues and biological functions, which will provide valuable guidance for the construction of bone tissue engineering (BTE) scaffolds.

## 1. Introduction

In orthopedic surgery, the scarcity of autologous bone remains a central issue that draws worldwide concern [1,2]. BTE scaffolds have risen as a promising solution to this challenge. The essence of BTE lies in the effective integration of three key elements: cells, scaffolds, and signals [3,4]. This convergence aims to develop biological substitutes designed for the restoration, maintenance, and replacement of damaged bone tissue [5]. Scaffolds are crucial in this field, offering the necessary physical support for the attachment and growth of BMSCs, which is essential for bone tissue formation [6]. Recently, with the growing adoption of the bottom-up approach, micron-sized scaffolds, termed microparticles, are emerging as multifunctional platforms that can recapitulate tissue heterogeneity in engineered cell microenvironments [7,8].

Microparticles offer numerous unique properties compared to traditional bulk materials, making them attractive for biomedical applications [9]. Firstly, the physical interactions within particle systems often result in shear-thinning behavior, which facilitates injection. This characteristic is advantageous for the minimally invasive delivery of

Peer review under the responsibility of KeAi Communications Co., Ltd.

* Corresponding authors.
** Corresponding author.
*** Corresponding authors.
**** Corresponding author.
*E-mail addresses:* sudaxk@163.com (K. Xi), zyr13579@hotmail.com (Y. Zhu), guyongsuzhou@163.com (Y. Gu), chenliang1972@sina.com (L. Chen).
[1] These authors contributed equally to this work.

https://doi.org/10.1016/j.bioactmat.2025.02.032
Received 22 October 2024; Received in revised form 15 February 2025; Accepted 19 February 2025

cells and bioactive agents [10]. Secondly, the modular nature of microparticle systems allows for the separation of mechanical and biochemical cues. Individual microparticles can present cells with distinct biochemical and mechanical signals in a spatiotemporal manner within the repair site [7]. Thirdly, the high specific surface area of microparticle systems provides an expanded space for cell expansion and nutrient exchange, enabling high-density cell culture and delivery [11]. In recent years, microparticles of predefined shapes and sizes have become accessible using a variety of fabrication techniques (such as batch emulsion, microfluidics, lithography, electrohydrodynamic spraying, and mechanical fragmentation) [9,12]. The range of microparticle shapes has expanded beyond conventional microspheres to include novel forms such as porous microspheres, microcapsules, and microrods [13,14]. However, in the current design and manufacturing processes of BTE scaffolds, the influence of topological cues from different microparticles on cell function tends to be overlooked.

Topological cues, which refer to the morphology and structural features of materials at the micron and nano scales, play a pivotal role in cell biology [15,16]. Recent studies have demonstrated that these cues can significantly influence cellular behavior through a variety of mechanisms, including mechanotransduction, receptor-mediated signaling pathways, metabolic remodeling, and epigenetic modifications [17,18]. For example, Song Li and colleagues found that oriented microgroove structures can modify cell nuclear morphology, thereby increasing chromatin accessibility and promoting the expression of pluripotency genes in stem cells [19]. Furthermore, recent studies have shown that micropatterned structures can enhance the nuclear localization of transcription factors like β-catenin, and YAP in stem cells through the transmission of mechanical signals, subsequently boosting stem cell metabolism and paracrine function [20,21]. Therefore, understanding how different topological cues presented by microparticles affect cellular behavior is essential. Such insights will not only deepen our understanding of microparticle systems but also greatly inform the design and fabrication of BTE scaffolds.

MPs and PMPs are the two most widely used microparticles in the field of BTE. Building on their properties, a multitude of functionalized scaffolds have been developed by adjusting material compositions, incorporating bioactive drugs, and modifying surfaces to achieve precise regulation of the biological behavior of BMSCs [22,23]. Despite the notable differences in topological cues between MPs and PMPs, research into how these variations impact BMSCs has been limited. Therefore, more in-depth studies should be performed to identify the differences in cellular responses to MPs and PMPs, which will help predict the biological effects that may be triggered in vivo, and thus accurately guide tissue regeneration.

In this study, we investigated the effects of PMPs and MPs on the function of BMSCs from multiple perspectives and explored the underlying molecular mechanisms with the aid of RNA-seq technology. Initially, we prepared PMPs and MPs using polylactic acid (PLA) and fibronectin (FN) for BMSCs culture. Cellular experiments revealed that BMSCs cultured with PMPs exhibited enhanced activity in proliferation, osteogenesis, paracrine effects, and energy metabolism. Subsequently, RNA-seq analysis unveiled the mechanistic pathways: PMPs activated the FAs signaling pathway in BMSCs, which led to the reorganization of intracellular mechanics and the nuclear translocation of the YAP protein, thereby enhancing BMSCs functionality (Fig. 1). Finally, using a rat femoral condyle defect model, we further demonstrated that BMSCs delivered with PMPs in vivo can significantly promote bone defect repair, highlighting their substantial potential as a cell carrier in BTE. In conclusion, this study provides a comprehensive and reliable understanding of the cellular interactions with MPs and PMPs. It underscores the significant potential of topological cues in the regulation of stem cell fate. We believe that our findings will provide valuable insights for the design and manufacture of microparticle-based BTE scaffolds.

## 2. Materials and methods

### 2.1. Preparation of PMPs and MPs

We initiated the process by preparing a 10 % (w/v) solution of PLA (Daigang, Jinan, Shandong, China) in dichloromethane (Aladdin, Shanghai, China). Concurrently, a 1 % (w/v) aqueous solution of gelatin

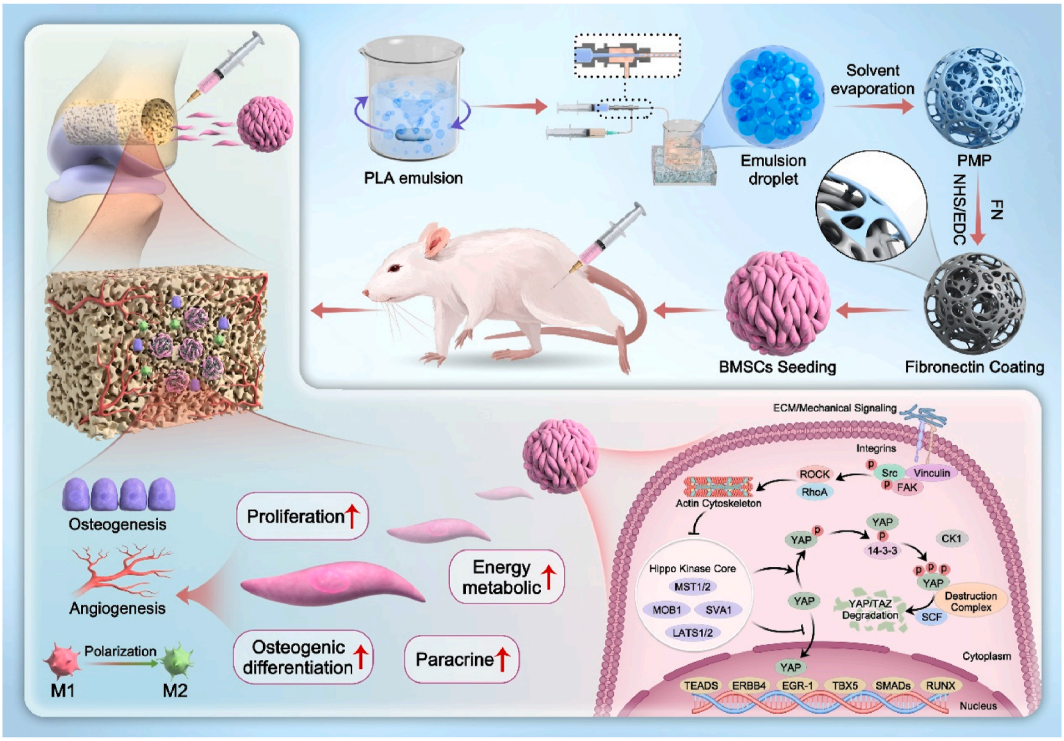


**Fig. 1.** A schematic illustration of how PMPs enhance the function of BMSCs to promote bone regeneration.

(Aladdin, Shanghai, China) was formulated. These solutions were meticulously blended in a 3:1 volumetric ratio to form a stable emulsion through the application of ultrasonication. In parallel, a 1 % (w/v) solution of polyvinyl alcohol (PVA; Sigma-Aldrich, St. Louis, MO, USA) was prepared, designated for use as the continuous phase within the microfluidic device. The emulsion, serving as the dispersed phase, was connected to the device, and the flow rate ratio between the continuous and dispersed phases was finely adjusted to 80:1. This precise adjustment facilitated the generation of monodisperse emulsion droplets with the targeted size. The droplets were then gently stirred overnight in an ice-water bath, allowing for the complete evaporation of dichloromethane and resulting in the formation of PLA/gelatin composite microspheres. These were subsequently subjected to three cycles of washing in 37 °C warm water to meticulously eliminate the internal gelatin, yielding PMPs. To obtain MPs, the initial emulsion was replaced with a pure PLA dichloromethane solution, adhering to the established protocol.

### 2.2. Modification of PMPs and MPs

Take 5 ml of 2-(N-Morpholino)-ethanesulfonic acid buffer solution (SinoDetech, Beijing, China) with a pH of 6 and add 40 mg of 1-(3-Dimethylaminopropyl)-3-ethylcarbodiimide (EDC; Beyotime, Shanghai, China) and N-Hydroxysuccinimide (NHS; Beyotime, Shanghai, China) respectively to configure the reaction solution. Weigh 1 g of freeze-dried MPs or PMPs and incorporate them into the reaction system. Stir the reaction mixture at room temperature overnight to ensure the complete activation of the carboxyl groups. On the following day, remove the reaction solution, add 5 ml of 1 mg/ml FN (Yeason, Shanghai, China) solution for grafting. React at room temperature overnight, collect the samples and rinse them three times with deionized water.

### 2.3. Scanning electron microscope (SEM) detection

#### 2.3.1. Observation of material morphology

The samples were mounted onto the sample stage using conductive tape, followed by gold sputter coating for 45 s. The morphology was subsequently observed using SEM (Hitachi, Tokyo, Japan) at an acceleration voltage of 10 kV. The elemental composition differences before and after FN grafting were analyzed via energy-dispersive X-ray spectroscopy.

#### 2.3.2. Cell adhesion morphology observation

100 microspheres were added to each well of a 24-well plate and 20,000 cells were seeded. After 1 day of culture, the culture medium was discarded. The wells were rinsed three times with phosphate buffered saline (PBS) at 37 °C, then fixed with 4 % paraformaldehyde at room temperature for 20 min. The paraformaldehyde was discarded and the wells were rinsed three times with deionized water. The samples were then dehydrated through an alcohol gradient. After dehydration, a critical point dryer was used to remove the alcohol, followed by gold spraying. Finally, the cell morphology and adhesion were observed under a SEM.

### 2.4. Atomic force microscopy (AFM) detection

#### 2.4.1. Analysis of surface roughness of materials

The surface morphology and roughness of MPs and PMPs before and after modification with FNs were detected using AFM (Bruker, Billerica, MA, USA) in non-contact mode. After scanning, NanoScope analysis software was used to generate topography maps and roughness reports of the detection area.

#### 2.4.2. Analysis of mechanical property of materials

The Young's modulus of MPs and PMPs was measured and analyzed by AFM under the derjaguin-muller-toporov (DMT) model. According to the Hertz model, the NanoScope analysis software was used to calculate each force-separation curve to obtain the Young's modulus at each detection point, and the Young's modulus distribution map within the detection area was drawn based on the corresponding results.

### 2.5. Detection of protein adsorption capacity

Prepare a 1 % solution of bovine serum albumin labeled with fluorescein isothiocyanate (FITC-BSA). Then, weigh 100 mg of FN-modified PMPs and MPs respectively and immerse them in the above solution for overnight incubation. The next day, collect the microspheres and wash them with deionized water. Observe and record the images under a fluorescence microscope. Finally, the ImageJ software was used to perform semi-quantitative analysis of the fluorescence intensity to evaluate the adsorption capacity of the microspheres for protein molecules.

### 2.6. Cell culture

All cell types used in this study were purchased from Cyagen Biosciences Inc (Suzhou, Jiangsu, China), and were cultivated in a humidified environment with 5 % carbon dioxide and maintained at a constant temperature of 37 °C.

#### 2.6.1. Cultivation of BMSCs

Rat BMSCs were nurtured in anti-cell adhesion well plates (EFL, Suzhou, Jiangsu, China), serving as culture containers, and co-cultured with microparticles in α-medium (Cyagen, Suzhou, Jiangsu, China) containing 10 % fetal bovine serum (FBS; Cyagen, Suzhou, Jiangsu, China) and 1 % penicillin-streptomycin (Gibco, Carlsbad, CA, USA). For the observation of osteogenic differentiation of BMSCs, an osteogenic induction medium was utilized for culture, comprising a high glucose dulbecco's modified eagle medium (DMEM; Cyagen, Suzhou, Jiangsu, China), supplemented with 10 mM β-glycerophosphate (Sigma-Aldrich Corp, St. Louis, MO, USA), 10 nM dexamethasone (Sigma-Aldrich Corp, St. Louis, MO, USA), and 50 μg/ml ascorbic acid (Sigma-Aldrich Corp, St. Louis, MO, USA).

#### 2.6.2. Cultivation of endothelial cells (ECs) and RAW264.7 cells

In this experiment, we prepared conditioned media (CM) for culturing ECs and RAW264.7 cells. The preparation procedure was as follows: Firstly, 1g of PMP or MP was co-cultured with 1,000,000 BMSCs in serum-free medium. After a 1-day incubation period, the culture medium was collected and centrifuged at 2000 rpm for 10 min to remove residual cellular debris, yielding the supernatant. This supernatant was then mixed with high-glucose complete medium at a 1:1 ratio to generate the CMs. Depending on the type of co-culture substrate, the CMs were designated as PMP-CM and MP-CM, respectively. It is worth noting that during the culturing process of RAW264.7 cells, 200 ng/ml lipopolysaccharide (LPS; Beyotime, Shanghai, China) needs to be added to the culture medium to simulate the inflammatory environment.

#### 2.6.3. The use of inhibitors and agonists in cell culture processes

In the experiment, various small molecule inhibitors and agonists were used. The corresponding application time and concentration are as follows. RGD peptide (MCE, New Jersey, USA) and Pyintegrin (MCE, New Jersey, USA) were dissolved in the culture medium to a concentration of 20 μM, and BMSCs were treated for 7 days before WB detection of the contents of phosphorylated focal adhesion kinase (pFAK), G-actin, phosphorylated myosin light chain (pMLC), YAP, pYAP, and Lamin A/C in the cells. Verteporfin (MCE, New Jersey, USA) and PY60 (MCE, New Jersey, USA) were dissolved in the culture medium to a concentration of 10 μM for the culture of BMSCs. Ki67 flow cytometry was performed after 5 days of culture. WB detection of mitofusin 1 (MFN1), mitofusin 2 (MFN2), and dynamin-related protein 1 (DRP1), glucose transporter 1

(GLUT1), hexokinase 2 (HK2), ATP synthase F1 subunit-α (ATP5A), cytochrome *c* oxidase subunit 4I1 (COX4I1), ubiquinone oxidoreductase subunit B8 (NDUFB8), ubiquinol-cytochrome c reductase core protein 1 (UQCRC1), and succinate dehydrogenase complex flavoprotein subunit A (SDHA) was conducted after 7 days of culture. Runt-related transcription factor 2 (RUNX2) was detected by WB after 14 days of culture. Osteopontin (OPN) was detected after 28 days of culture.

### 2.7. Cell proliferation test

The bottom of each well in the 96-well plates was covered with PMPs or MPs, and then 4000 BMSCs were added to each well for co-culture. On the 1st, 3rd, and 5th days post-culture, the culture medium was replaced with medium containing 10 % cell counting kit-8 (CCK-8) working solution (Beyotime, Shanghai, China). After a 2-h incubation, the optical density (OD) value at a wavelength of 450 nm was detected using a microplate reader (Thermo Fisher Scientific, Waltham, MA, USA).

### 2.8. Live/dead cell staining

The bottom of each well in the 24-well plates was covered with PMPs or MPs, followed by the addition of 10,000 BMSCs for co-culture. After 7 days of incubation, the culture medium was carefully aspirated and the wells were washed with PBS to eliminate residual esterase activity. 500 μl of the pre-prepared Calcein-AM/PI working solution (Beyotime, Shanghai, China) was added to each well and incubated for 30 min. Live cells, which exhibit yellow-green fluorescence, and dead cells, which display red fluorescence, were observed using a confocal microscope (Carl Zeiss AG, Oberkochen, Germany).

### 2.9. ALP and ARS staining

The bottom of each well in the 24-well plates was covered with PMPs or MPs, followed by the addition of 10,000 BMSCs for co-culture. When the cell growth density reaches 80 %, switch to osteogenic induction medium for culture, and replace the medium every two days during this period. On the 7th day, the expression of alkaline phosphatase (ALP) was detected using the BCIP/NBT kit (Jiancheng, Nanjing, Jiangsu, China). On the 14th day post-induction, calcium nodules were marked with alizarin red (ARS; Cyagen, Suzhou, China) for observation under a microscope. The nodules were then dissolved with perchloric acid (Aladdin, Shanghai, China), and the absorbance at a 540-nm wavelength was measured.

### 2.10. Flow cytometry detection

In the experiment, BMSCs were collected for Ki67 detection after 5 days of culture, while RAW264.7 cells were collected for CD11b, CD206, and CD86 detection after 3 days of culture. The collected cells were fixed with paraformaldehyde (Yeason, Shanghai, China), then washed and incubated with the corresponding primary antibodies for 1 h. After further centrifugation and washing, they were incubated with IgG-FITC (Thermo Fisher Scientific, Waltham, MA, USA) in the dark for 30 min. Subsequently, the cells were centrifuged, rinsed, resuspended, and analyzed by flow cytometry.

### 2.11. Immunofluorescence staining

In this experiment, the fluorescence of multiple proteins was detected, and the corresponding detection time points are presented as follows. Regarding the staining of osteogenesis-related proteins, RUNX2 staining was conducted 14 days after culture, OPN and osteocalcin (OCN) was performed 28 days after culture. The detection time points for integrin-β1, vinculin, and YAP were chosen 7 days after co-culture with microspheres.

Upon collecting the cultured cells at the aforementioned time points, the cells were fixed, infiltrated, blocked, and washed. Subsequently, primary antibodies such as RUNX2, OPN, OCN, integrin-β1, vinculin, YAP, etc. were added and incubated overnight. Then, they were incubated with secondary antibodies at room temperature for 2 h. After staining with phalloidin (Yeason, Shanghai, China) and 4′,6-diamidino-2-phenylindole (DAPI; Yeason, Shanghai, China), observations were made under a confocal microscope. Cell counts were carried out using ImageJ to detect the number of cells in each immunofluorescence image. Semi-quantitative fluorescence analysis was implemented with ImageJ software. The integrated fluorescence intensity was divided by the cell count in each image to obtain the standardized immunofluorescence intensity. All antibodies used in the experiment were purchased from ABclonal Biotechnology Co. Ltd (Shanghai, China).

### 2.12. Western blot (WB) analysis

In this experiment, cell samples were collected at specific time points for the detection of target proteins. RUNX2 was detected after 14 days of culture, while OPN was detected after 28 days. After a 7-day culture, the following proteins were detected: proteins related to cell mechanics, including pFAK, G-actin, pMLC, YAP, pYAP, and lamin A/C; proteins related to mitochondrial dynamics, including MFN1, MFN2, and DRP1; proteins related to glycolysis, including GLUT1 and HK2; proteins related to oxidative phosphorylation, including ATP5A, COX4I1, NDUFB8, UQCRC1, and SDHA. Proteins related to the MAPK pathway, such as p38 mitogen-activated protein kinase (p38), phospho-p38 mitogen-activated protein kinase (p-p38), extracellular signal-regulated kinase (ERK), phospho-extracellular signal-regulated kinase (p-ERK), c-Jun N-terminal kinase (JNK), and phospho-c-Jun N-terminal kinase (p-JNK); proteins related to the PI3K-AKT pathway, such as protein kinase B (AKT) and phospho-protein kinase B (p-AKT).

After collecting the cell samples, 400 μL of complete lysis buffer (Beyotime, Shanghai, China) was added for processing. Following cell lysis, centrifugation was performed at 4 °C and 12,000 rpm to obtain the supernatant, which constituted the total protein solution. The bicinchoninic acid protein assay kit (Beyotime, Shanghai, China) was utilized to measure the protein concentration of each group's solution, standardizing them to a uniform level. The extracted proteins were resolved by gel electrophoresis and then transferred onto a polyvinylidene fluoride membrane (Millipore Corp, Billerica, MA, USA). The membrane was blocked with blocking buffer (Beyotime, Shanghai, China) for 15 min, followed by an overnight incubation with the respective primary antibodies. On the subsequent day, the membrane was washed three times with tris-buffered saline with tween-20 (Beyotime, Shanghai, China) and incubated with horseradish peroxidase conjugated IgG (Beyotime, Shanghai, China) for 1 h at room temperature. Finally, the membrane was treated with chemiluminescent substrate, and the bands were visualized and quantified using an imaging system (Baygene, Hongkong, China). The gray values of the bands were determined using ImageJ software, and the ratio of the band gray values to the internal reference bands was calculated.

### 2.13. ECs migration experiment

ECs were plated at a density of 50,000 cells per well in 24-well plates and cultivated in standard high-glucose medium until they reached a confluence of 90 %. A scratch was introduced using a 200 μl pipette tip to create a wound, after which non-adherent cells were removed by rinsing with PBS. Subsequently, the cells were treated with both standard high-glucose medium and distinct conditioned media for a duration of 24 h. The progression of wound closure was documented via microscopic imaging, and the extent of scratch healing was quantitatively evaluated using ImageJ software.

### 2.14. ECs tube formation experiment

The growth factor-reduced matrigel (Corning, New York, USA) was diluted to a 1:3 ratio with culture medium, and 30 μl of this dilution was evenly applied to the bottoms of pre-chilled 24-well plates to form a gel layer, which was then incubated at 37 °C for 30 min to solidify. ECs were seeded into the plates at a density of 10,000 cells per well and cultured in various media. After a 9-h incubation period, images were captured using a microscope, and the images were analyzed quantitatively using ImageJ software.

### 2.15. Enzyme-linked immunosorbent assay (ELISA) detection

After co-culturing BMSCs with PMPs or MPs for 1 day, the culture medium was collected and centrifuged at 2000 rpm for 10 min to obtain the supernatant. The concentrations of vascular endothelial growth factor A (VEGFA) and transforming growth factor-β (TGF-β) in the supernatant were measured using ELISA kits (Anogen, Mississauga, Ontario, Canada). Similarly, RAW264.7 cells were cultured in different media for 3 days, after which the levels of interleukin-1β (IL-1β), tumor necrosis factor-alpha (TNF-α), interleukin-4 (IL-4), and interleukin-10 (IL-10) in the culture media were determined.

### 2.16. ATP assay kit

After co-culturing 10,000 BMSCs with 100 microspheres in each well of a 24-well plate for 7 days, the cells were collected and treated with 200 μL of lysis buffer to ensure complete cell lysis. The mixture was then centrifuged at 4 °C and 12,000 rpm for 5 min to obtain the supernatant. Next, 40 μl of the supernatant was combined with 100 μl of adenosine triphosphate (ATP) detection reagent (Beyotime, Shanghai, China) in a white-walled 96-well plate. The relative light units were measured using a luminometer, and the ATP concentrations of the samples were determined using a standard curve.

### 2.17. Extracellular acidification rate (ECAR) and oxygen consumption rate (OCAR) assays

BMSCs cultured under various conditions were harvested and replated at a density of 10,000 cells per well in the XFe24 plate (Agilent Technologies, Palo Alto, CA, USA). The culture medium was replaced with 175 μl of complete Seahorse assay medium and incubated at 37 °C for 1 h. To measure the OCR, 2 μM oligomycin, 2 μM carbonyl cyanide 4-(trifluoromethoxy)-phenylhydrazone (FCCP), and 1 μM rotenone/antimycin were injected into the sensor cartridge ports. For the ECAR measurement, 10 mM glucose, 2 μM oligomycin, and 2 μM 2-deoxy-D-glucose (2-DG) were injected into the sensor cartridge ports. The cell plate and sensor cartridge were then analyzed using the Seahorse XFe24 bioanalyzer (Agilent Technologies, Palo Alto, CA, USA) to obtain OCR and ECAR results.

### 2.18. Transmission electron microscopy (TEM)

Cells were fixed in the dark with precooled 2.5 % glutaraldehyde (Yeason, Shanghai, China). The samples were stored on ice at 4 °C and then shipped to Hangzhou Yanqu Information Technology Co. Ltd (Hangzhou, Zhejiang, China) for further embedding, sectioning, and staining processes. Mitochondrial and nuclear pore morphologies were observed under a TEM (JEOL, Tokyo, Japan), and images were collected. Finally, quantitative analysis was performed using ImageJ software.

### 2.19. RNA-seq analysis

After 7-days co-culture of BMSCs with PMP or MPs, the cells were digested and collected by trypsin (Cyagen, Suzhou, China), and RNA was extracted using Trizol reagent (Cyagen, Suzhou, China). The purity and quantity of RNA were measured and quantified using a Nano Drop 2000 spectrophotometer. Transcriptome sequencing and analysis were conducted by OE Biotech Co. Ltd (Shanghai, China). The original sequencing reads were analyzed and obtained using Trimmomatic and hisat2 software. Cufflinks software was utilized to quantify the obtained base fragments. Gene Ontology (GO) and kyoto encyclopedia of genes and genomes (KEGG) enrichment analysis was performed on differentially expressed genes with a p-value less than 0.05 and a fold change greater than 1.5 to determine the main biological functions or pathways affected by the differentially transcribed transcripts. Hierarchical clustering of differentially transcribed transcripts was performed using a heatmap to study the expression patterns among different samples.

### 2.20. Establishment of animal models

Male SD rats weighing 250–300 g purchased from Experimental Animal Center of Soochow University were used to create a femoral condyle defect model. The rats were anesthetized by intraperitoneal injection of 2 % pentobarbital sodium at a dosage of 2.5 mL/kg. The skin was incised, and the deep fascia was separated to expose the femoral condyles. A 3 mm drill bit was used to create holes on both sides of the femoral condyles. PMPs and MPs carrying cells were implanted to simulate the defect repair process. Rats that were injected with only normal saline in the defect area served as the control group. The wounds were closed in layers, and penicillin was administered daily for 3 days postoperatively to prevent infection. Rats from different groups were euthanized at 2 and 4 weeks postoperatively, and femur specimens were collected and fixed in 4 % paraformaldehyde.

### 2.21. Detection and reconstruction of Micro-CT

Micro-CT (Bruker, Billerica, Massachusetts, USA) scanning was utilized to evaluate the healing of femoral defects, with specific operational parameters including a spatial resolution of 18 μm, an X-ray tube voltage of 65 kV, and a current of 385 mA. At the center of the defect area, a cylindrical region of interest (ROI) with a diameter of 3 mm was selected. Quantitative analysis was performed on the following indices using DataView and CT analysis software: Bone Mineral Density (BMD), Bone Volume to Total Volume ratio (BV/TV), Trabecular Separation (TB.sp), and Trabecular Thickness (TB.th). The data obtained from the analysis were presented in the form of histograms and were subjected to statistical analysis to assess the differences among various groups.

### 2.22. Histological section detection

The collected specimens were decalcified with a 10 % EDTA solution (Thermo Fisher Scientific, Waltham, MA, USA), dehydrated through an ethanol gradient, and embedded in paraffin. Sagittal sections of the femur were prepared, and tissue regeneration and new bone conditions in the defect area were examined using hematoxylin and eosin (H&E) staining and Masson's trichrome staining. Immunofluorescence staining for OCN, OPN, CD31, Arginase-1 (Arg-1), and Inducible Nitric Oxide Synthase (iNOS) was performed on the tissue sections to evaluate osteogenic differentiation, angiogenesis, and local immune remodeling. All antibodies used in the experiment were purchased from ABclonal Biotechnology Co. Ltd (Shanghai, China).

### 2.23. Statistical analysis

All experimental data are presented as mean ± standard deviation. Statistical analysis and plotting were performed using Origin 9.1 or GraphPad Prism 7.0 software. One-way or two-way ANOVA followed by Tukey's test was used to determine statistical significance, with $p < 0.05$ considered statistically significant.

## 3. Results and discussion

### 3.1. Preparation and characterization of PMPs and MPs

As shown in Fig. 2A, this study used PLA and FN to prepare MPs and PMPs. The size distribution of the emulsion droplets (PMPs precursors) and the solution droplets (MPs precursors) was 406.4 ± 18.83 μm and 423.3 ± 35.74 μm, respectively (Fig. 2B–D). We systematically assessed the distribution of Young's modulus in specific areas of the surfaces of PMPs and MPs by means of AFM indentation (Fig. S1A). The results

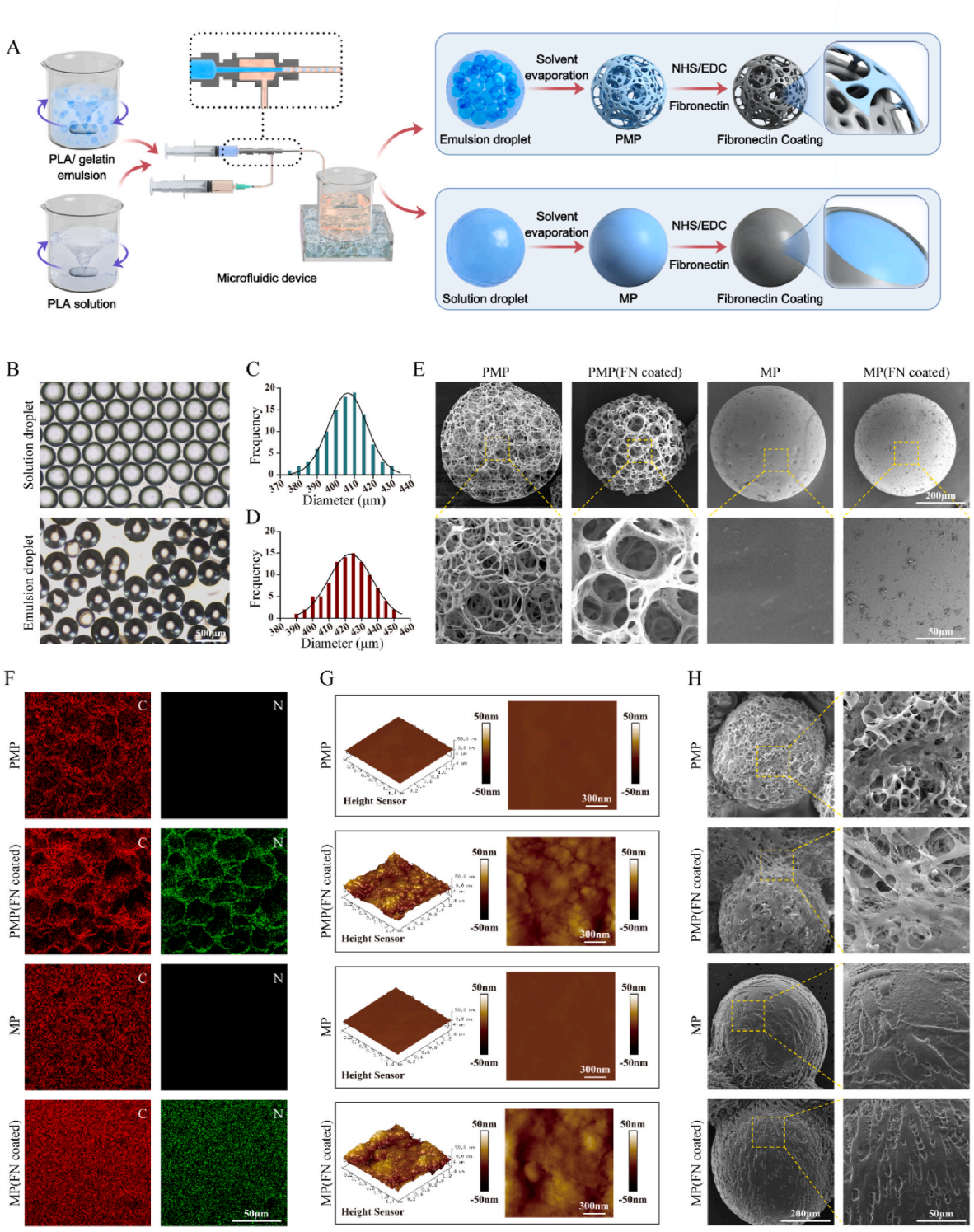


**Fig. 2.** Preparation of PMPs and MPs based on PLA and FN. A) Schematic diagram of the preparation process for PMPs and MPs; B) Microscope morphology of solution droplets and emulsion droplets; C) Frequency distribution histogram of solution droplet sizes (n = 100); D) Frequency distribution histogram of emulsion droplet sizes (n = 100); E) SEM morphology of PMPs and MPs with or without FN coating; F) Element mapping detection of carbon and nitrogen elements on the surface of PMPs and MPs with or without FN coating; G) Changes in surface roughness of PMPs and MPs with or without FN coating observed by AFM; H) Cell adhesion on PMPs and MPs with or without FN coating observed by SEM.

demonstrated that, owing to the porous structure, PMPs manifested significant variations in Young's modulus in different regions. By computing the average Young's modulus within the detection area to characterize the overall mechanical properties of the microspheres (Fig. S1B), we discovered that the Young's modulus of the PMPs decreased conspicuously under the influence of the pore structure. Nevertheless, it is noteworthy that the Young's modulus of PMPs still reached 3.789 GPa, suggesting that the PMPs possess excellent mechanical properties. In biological environments, materials adsorb proteins from their surroundings onto their surfaces, forming a protein adsorption layer [24]. Consequently, the interaction between cells and materials at the interface can be described as the interaction between cells and the surface-bound proteins [25]. In this study, our objective is to explore the effects of topological differences between PMPs and MPs on cell behavior. To mitigate the impact of variations in the protein adsorption layer on the experimental outcomes, we applied a FN coating to both PMPs and MPs. Therefore, after obtaining the corresponding microparticle samples, the FN was directly coated on its surface using the NHS/EDC coupling method. The element mapping results shown in Fig. 2F indicate that the nitrogen element distribution is uniform after the FN coating, consistent with the carbon element distribution, which indicates that a uniform FN coating has been formed on the surface of the microparticle. Through SEM observation, we observed significant changes in the microscopic morphology of both PMPs and MPs before and after the coating process (Fig. 2E). Further assessment using AFM revealed that the roughness average (RA) value of PMPs increased from 0.324 nm to 5.46 nm after coating. Similarly, the RA value of MPs increased from 0.407 nm to 7.08 nm (Fig. 2G). We employed a fluorescence microscope to observe the adsorption capacity of FITC-labeled BSA by MPs and PMPs after coating treatment, which could reflect their adsorption capability for bioactive factors. In the experiment, we discovered that there was no significant disparity in fluorescence intensity between MPs and PMPs (Figs. S2A and B), which can ensure there will be no inter-group differences caused by local cytokine concentration variations. We consider this to be mainly attributed to the following two aspects. Firstly, from the perspective of physical adsorption, in accordance with the principle of the molecular sieve effect, the adsorption capacity of porous materials is the strongest when the pore size is commensurate with the size of the adsorbate molecules [26]. In this experiment, the average pore size of porous microspheres was approximately 40 μm (Fig. S2C), while the diameter range of protein molecules was 1–100 nm. Herein, the considerable size difference results in the incapability of PMPs to effectively retain the protein molecules captured by the material surface, thereby significantly reducing their adsorption capacity for proteins. Secondly, the same FN coating modification was conducted on the two types of microspheres, which would introduce protein binding sites (the 12–14 type repeat sequence domain of FN) of the same density onto the surfaces of the two types of microspheres [27]. As a result, PMPs and MPs microspheres acquired similar chemical adsorption capabilities, which further mitigated the disparity in protein adsorption capacity between them. Ultimately, we assessed the adhesion of BMSCs on both PMPs and MPs, with and without FN coating, using SEM following a 1-day co-culturing period (Fig. 2H). Our findings indicated that the FN coating substantially improved cell adhesion on the material surfaces. Notably, the FN coating also minimized the disparity in cell adhesion between the PMP and MP groups when compared to their uncoated counterparts.

### 3.2. The influence of PMPs and MPs on the cellular behavior of BMSCs

BMSCs are widely present in adult bone marrow and possess five key characteristics: self-renewal, low immunogenicity, high activity, pro-inflammatory response, and non-tumorigenic properties. These attributes make them the most widely used seed cells in bone tissue engineering [28,29]. In the process of bone repair, BMSCs play a central role. On one hand, they directly contribute to bone tissue repair through their own osteogenic differentiation [30]. On the other hand, they regulate various repair cells, including ECs and inflammatory cells, in the injured area through paracrine action, thereby reshaping the local repair microenvironment [31–33]. Consequently, in this section, we explored the effects of MPs and PMPs on BMSCs' function from the perspectives of proliferation, osteogenic differentiation, paracrine action, and energy metabolism.

#### 3.2.1. Proliferation and osteogenesis

We first examined the viability and proliferation of the cells in each group. Through live/dead staining detection, we observed that BMSCs in both PMPs and MPs exhibited high cell viability (Fig. 3A). We then performed proliferation assays using the CCK-8 assay kit on days 1, 3, and 5 for both groups. The results showed no significant difference in cell proliferation between the two groups on day 1; however, PMP group showed a remarkable increase on days 3 and 5 (Fig. 3B). From a holistic perspective, cell proliferation depends on the number of cells in synthesis phase (S phase), during which Ki67 protein is highly expressed in the nucleus [34]. We conducted an analysis of the Ki67-positive ratio in the two cell groups using immunofluorescence staining and flow cytometry. Our results revealed that BMSCs cultured on PMPs exhibited a significantly higher Ki67-positive ratio (Fig. 3C and D). Based on the above results, we concluded that the PMPs could induce more BMSCs to enter S phase, thereby promoting their proliferative ability.

We further compared the differences in osteogenesis between the two groups of cells. ALP is a glycoprotein secreted by osteoblasts, and its expression level reflects the cell's osteogenic activity [35]. As shown in Fig. S3, after a 7-day period of osteogenic induction, the ALP staining intensity in the PMP group was significantly higher than that observed in the MP group. This finding aligns with the outcomes of the quantitative ALP activity assay, indicating a stronger osteogenic response in the PMP group. Calcium nodules serve as markers for late osteogenic differentiation and were utilized to evaluate BMSCs' mineralization capacity [36]. After 14 days of induced differentiation, ARS staining and quantitative assay showed that BMSCs in PMP group demonstrated superior pro-mineralization ability over that of MP group (Fig. S3). RUNX2, a quintessential transcription factor, marks the early stages of osteogenic differentiation, orchestrating the development and functionality of osteoblasts. The expression levels of RUNX2 are pivotal, as they directly influence the commencement and advancement of osteogenesis. OPN and OCN emerge as significant matrix proteins in the later phases of osteogenic differentiation, exerting a critical impact on the mineralization process. Moreover, these proteins are indispensable for preserving the structural integrity and physiological function of bone tissue [37]. To delve deeper into the osteogenic activity of cells under varying culture conditions, we carried out fluorescence staining of RUNX2 on the 14th day and fluorescence staining of OPN and OCN on the 28th day (Fig. 3E and G and 3I). Upon evaluating the fluorescence intensity, it was observed that the PMP group exhibited significantly higher levels of these markers compared to the MP group, indicating a more robust osteogenic response in the PMP group (Fig. 3F and H and 3J). A similar trend was observed during subsequent WB assays: expression levels of RUNX2 (14th day) and OPN (28th day) were all elevated in the PMP group compared to those in the MP group (Fig. 3K–M).

#### 3.2.2. Paracrine effect

The paracrine signals of BMSCs play a key role in various biological processes related to bone tissue repair, especially angiogenesis and inflammatory resolution, demonstrating significant potential for bone regeneration [38]. To investigate the differences in paracrine signals of BMSCs in response to MPs and PMPs, we measured the levels of bioactive factors in the supernatants of BMSCs co-cultured with MPs or PMPs for 1 day. VEGFA expression and secretion play a crucial role in the cell-to-cell communication between BMSCs and ECs [39]. We quantitatively detected the VEGFA content in the supernatants using an ELISA kit and found that the average concentration of VEGFA in the PMP group

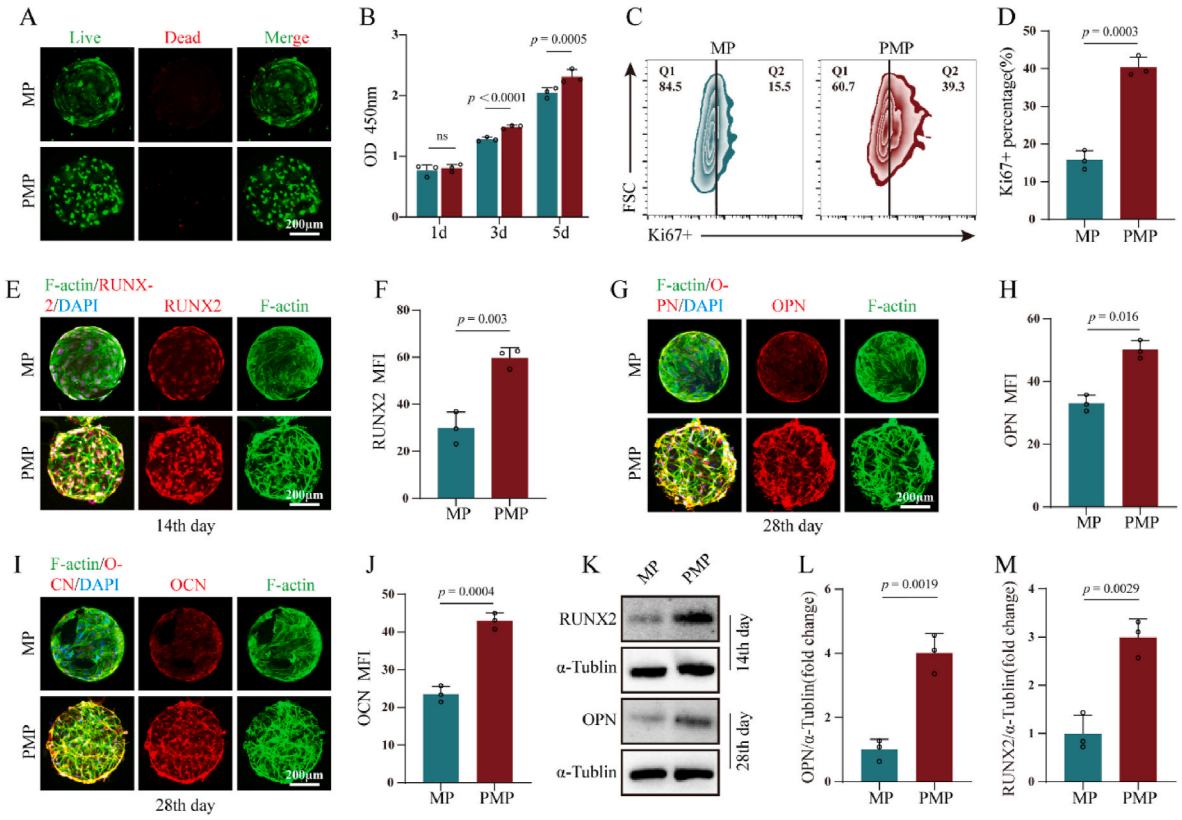


**Fig. 3.** Comparative analysis of the differences in the in vitro proliferation and osteogenic functions of BMSCs under the action of PMPs and MPs. A) Representative images of live/dead staining of BMSCs on PMPs or MPs surfaces; B) CCK-8 assay to detect the proliferation of BMSCs influenced by PMPs and MPs on days 1, 3, and 5 (n = 3); C, D) Representative images of flow cytometry detection of Ki67-positive BMSCs under the influence of PMPs and MPs and related statistical analysis (n = 3); E-J) Representative images of immunofluorescence for RUNX2, OPN, and OCN in BMSCs under the influence of PMPs and MPs and related statistical analysis of fluorescence intensity (n = 3); K-M) Representative Western blot bands and related statistical analysis of OPN and RUNX2 in BMSCs under the action of PMPs and MPs (n = 3).

was 48.71 pg/ml, which was 1.98 times higher than that in the MP group (Fig. S4A). TGF-β promotes the transformation of macrophages to an anti-inflammatory phenotype by inhibiting the activation of pro-inflammatory transcription factors AP-1, NF-κB, and STAT1 [40, 41]. In our experiment, we also found that TGF-β was significantly higher in the PMP group than in the MP group (Fig. S4B). Further, we observed significant differences in the morphology of BMSCs between the PMP and MP groups after 1 day of co-culture through F-actin staining. Specifically, BMSCs in the PMP group were more elongated, while those in the MP group were more flattened and spread out (Fig. S4C). Previous studies have indicated that changes in the morphological phenotype of BMSCs have a significant impact on their paracrine function. Therefore, we believe that PMPs reshape the morphology of BMSCs through their topological cues, thereby promoting the secretion of bioactive factors such as VEGFA and TGF-β.

As depicted in Fig. 4A, the collected supernatants were prepared as conditioned media (PMP-CM and MP-CM), respectively, for culturing ECs and RAW264.7 cells. Subsequently, the regulatory capabilities of BMSCs on angiogenesis and inflammation resolution in both groups were further observed. Angiogenesis plays an indispensable role in bone repair by supplying essential oxygen and nutrients to newly formed bone tissue while facilitating the clearance of metabolic waste, both of which are critical for cell survival and function [42–44]. It involves a series of cellular events, including the activation, proliferation, migration of ECs, and the formation of vascular networks [45]. We verified the differences between PMP-CM and MP-CM through proliferation, migration, and tube formation experiments. The CCK-8 results showed that PMP-CM significantly enhanced the proliferation of ECs compared to MP-CM (Fig. 4B). The scratch assay was used to detect the effect of these paracrine signals on cell migration. After treatment with PMP-CM, the scratch healing rate reached 74.24 % at 24 h, which was significantly higher than 55.27 % in the MP-CM group and 28.51 % in the Control-CM group (Fig. 4C and D). Finally, as shown in Fig. 4E, the formation of primitive vascular-like networks was significantly increased after 6 h of exposure to different media. Compared with Control-CM and MP-CM, the network structure induced by PMP-CM showed significant enhancements in tube length, tube number, and node number (Fig. 4F–H). In conclusion, under the influence of PMPs, the ability of BMSCs to secrete VEGFA was promoted, demonstrating a stronger capacity for angiogenesis regulation.

Inflammation is a dynamic process mediated by immune cells within the body [46], involving injury, anti-injury, and repair. Under normal circumstances, resident macrophages in tissues trigger and regulate this process. Currently, it is believed that the pro-inflammatory (M1) phenotype of macrophages can be transformed into an anti-inflammatory (M2) phenotype, promoting inflammation resolution, tissue remodeling, and new blood vessel formation, thereby accelerating wound healing [47]. After RAW264.7 cells were cultured in different media for 3 days, immunofluorescence showed that the fluorescence intensity of CD206 and Arg-1 in RAW264.7 cells treated with PMP-CM was the highest, while that of iNOS was the weakest (Fig. 4I and N); consistent results were obtained through flow cytometry analysis (Fig. S5). Finally, we detected the secretion of inflammatory factors (IL-1β and TNF-α) and anti-inflammatory factors (IL-4 and IL-10) in RAW264.7 cells under different culture systems (Fig. 4J–M). Compared with the Control-CM treatment group, both PMP-CM and MP-CM significantly reduced the secretion of IL-1β and TNF-α in RAW264.7 cells, while increasing the secretion of IL-4 and IL-10; compared with

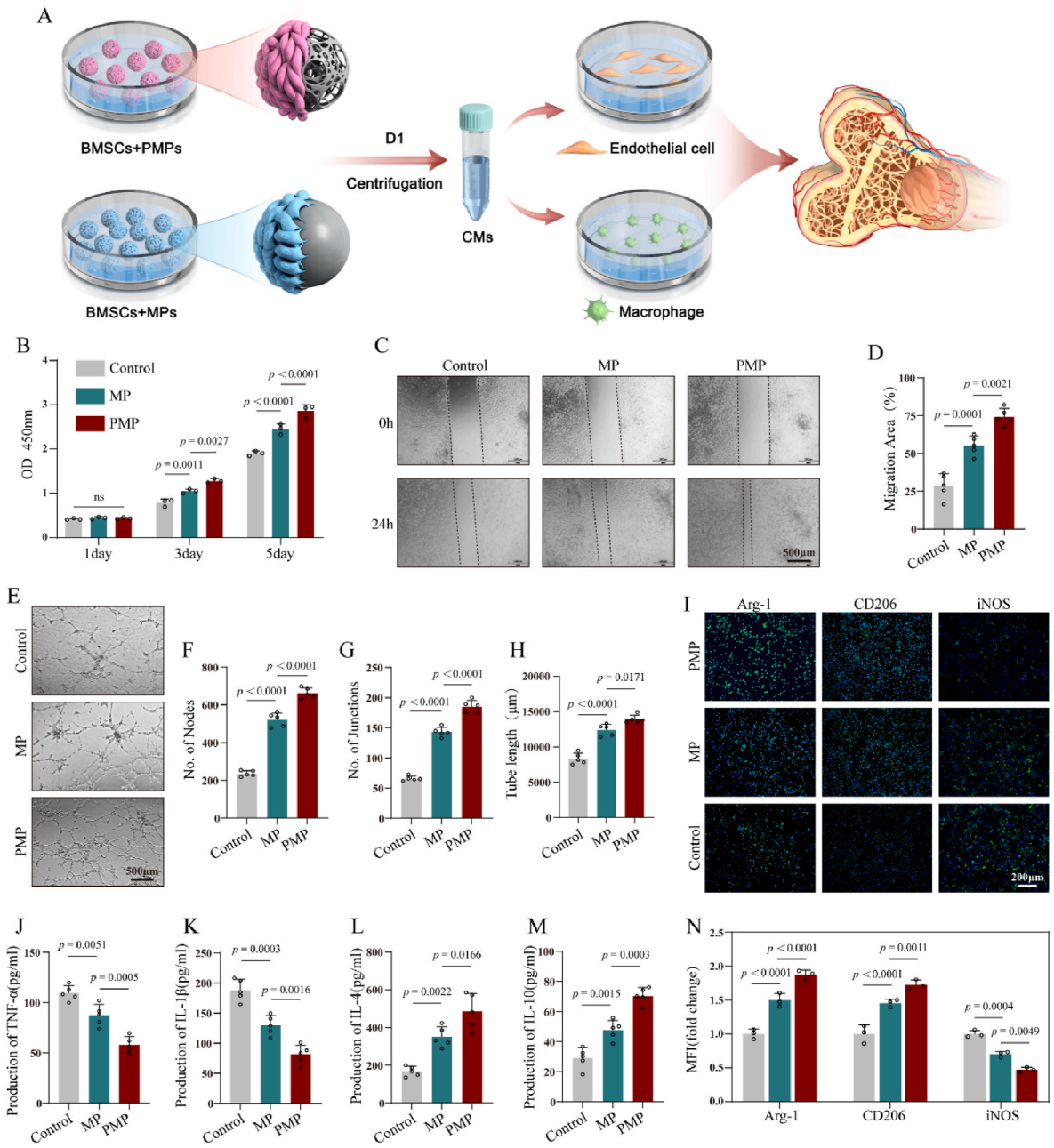


**Fig. 4.** Changes in paracrine function of BMSCs under the influence of PMPs and MPs. A) Schematic diagram of in vitro cell culture experiments to evaluate the impact of different conditioned media (CMs) on the behavior of resident cells in the skeletal microenvironment. B) CCK-8 assay to measure the proliferation of ECs treated with different CMs for 1, 3, and 5 days (n = 3); C, D) Scratch assay to observe the migration of ECs treated with different CMs at 0 and 24 h (n = 3); E-H) Representative images and quantitative analysis of tube formation in ECs treated with different CMs for 9 h (n = 5); I, N) Representative images and semi-quantitative analysis of immunofluorescence staining for iNOS, CD206, and Arg-1 in macrophages treated with different CMs for 3 day (n = 3); J-M) ELISA quantitative analysis of the production of pro-inflammatory cytokines (IL-1β and TNF-α) and anti-inflammatory cytokines (IL-4 and IL-10) in macrophages cultured with different CMs for 3 day (n = 5).

MP-CM, PMP-CM induced a more significant reduction in inflammatory factors and a more significant increase in anti-inflammatory factors. In conclusion, we believe that PMPs can effectively promote the synthesis and secretion of TGF-β in BMSCs and promote the transformation of macrophages to an anti-inflammatory phenotype.

### 3.2.3. *Glucose metabolism*

The maintenance of proliferation, osteogenic differentiation, and paracrine functions necessitates a substantial energy expenditure. Utilizing ATP assay kits, we discovered that BMSCs in the PMP group produced 1.8 times more ATP than those in the MP group (Fig. 5B). Glucose serves as the primary energy source for cells, producing ATP through glycolysis and oxidative phosphorylation to meet the energy demands. Seahorse real-time cell metabolism analysis was used to monitor the alterations in the glucose metabolism of BMSCs following exposure to PMPs and MPs. The research findings suggested that BMSCs exhibit a higher basal oxygen consumption and extracellular acidification rate in response to PMP (Fig. 5C–J), indicating increased activity of glycolytic and oxidative phosphorylation processes. Further Western blot (WB) experiments substantiated our findings, revealing that the

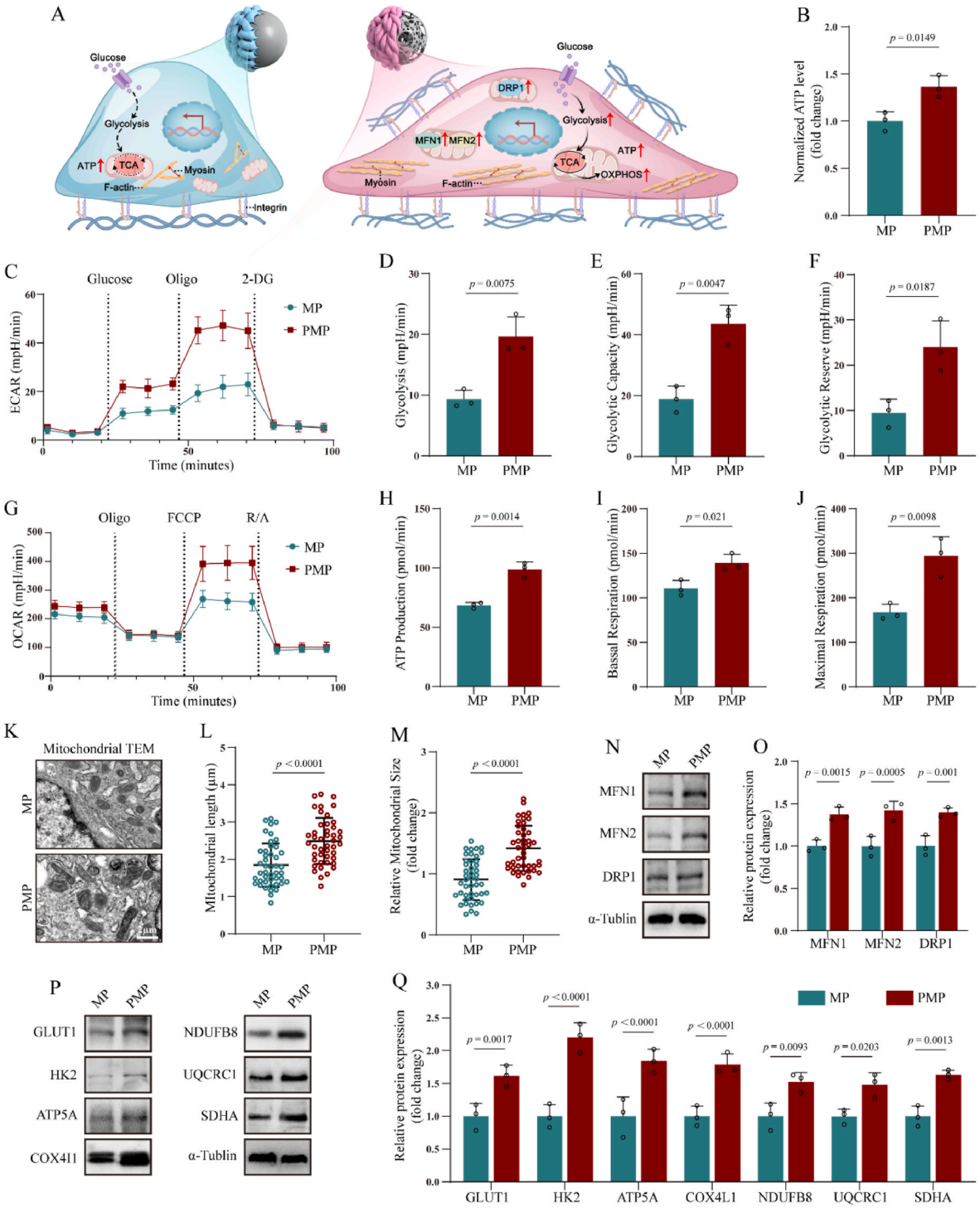


**Fig. 5.** Differences in glucose metabolic patterns of BMSCs under the action of PMPs and MPs. A) Schematic diagram of changes in mitochondrial dynamics and glucose metabolic patterns in BMSCs under the influence of MPs and PMPs; B) Statistical analysis of ATP generation in BMSCs affected by MPs or PMPs (n = 3); C-F) Seahorse assay results and statistical analysis of extracellular acidification rate (ECAR) in BMSCs under the influence of MPs or PMPs (n = 3); G-J) Seahorse assay results and statistical analysis of oxygen consumption rate (OCAR) in BMSCs under the influence of MP or PMP (n = 3); K-M) Representative TEM images of mitochondrial morphology in BMSCs under the influence of MPs or PMPs, and statistical analysis of mitochondrial length and size (n = 45); N, O) Representative Western blot bands and statistical analysis of mitochondrial dynamics-related proteins MFN1, MFN2, DRP1 in BMSCs under the influence of MPs or PMPs (n = 3); P, Q) Representative Western blot bands and statistical analysis of glucose metabolism-related proteins in BMSCs under the influence of MPs or PMPs.

PMP group exhibited higher expression levels of rate-limiting enzymes associated with glycolysis (GLUT1 and HK2) and subunit proteins that facilitate electron transfer during oxidative phosphorylation (ATP5A, UQCRC1, COX4I1, SDHA, and NDUFB8) [48] compared to the MP group (Fig. 5P and Q).

Mitochondrial dynamics refers to the process of maintaining the shape, distribution, number, and function of mitochondria through continuous fusion and fission [49]. We have observed an enhancement of oxidative phosphorylation and glycolysis processes in the PMP group, and an active mitochondrial dynamics process is the basis for supporting

high-intensity energy metabolism, so we further compared the differences in mitochondrial dynamics between the groups. We compared the lengths and areas of mitochondria in the two groups of cells using TEM. We observed that BMSCs exposed to PMP exhibited larger mitochondria (Fig. 5K). Specifically, the average length and area of these cells' mitochondria were 1.35 times and 1.57 times greater than those of the MP group, respectively (Fig. 5L and M). Based on these findings, we postulate that the presence of PMP leads to an inclination of

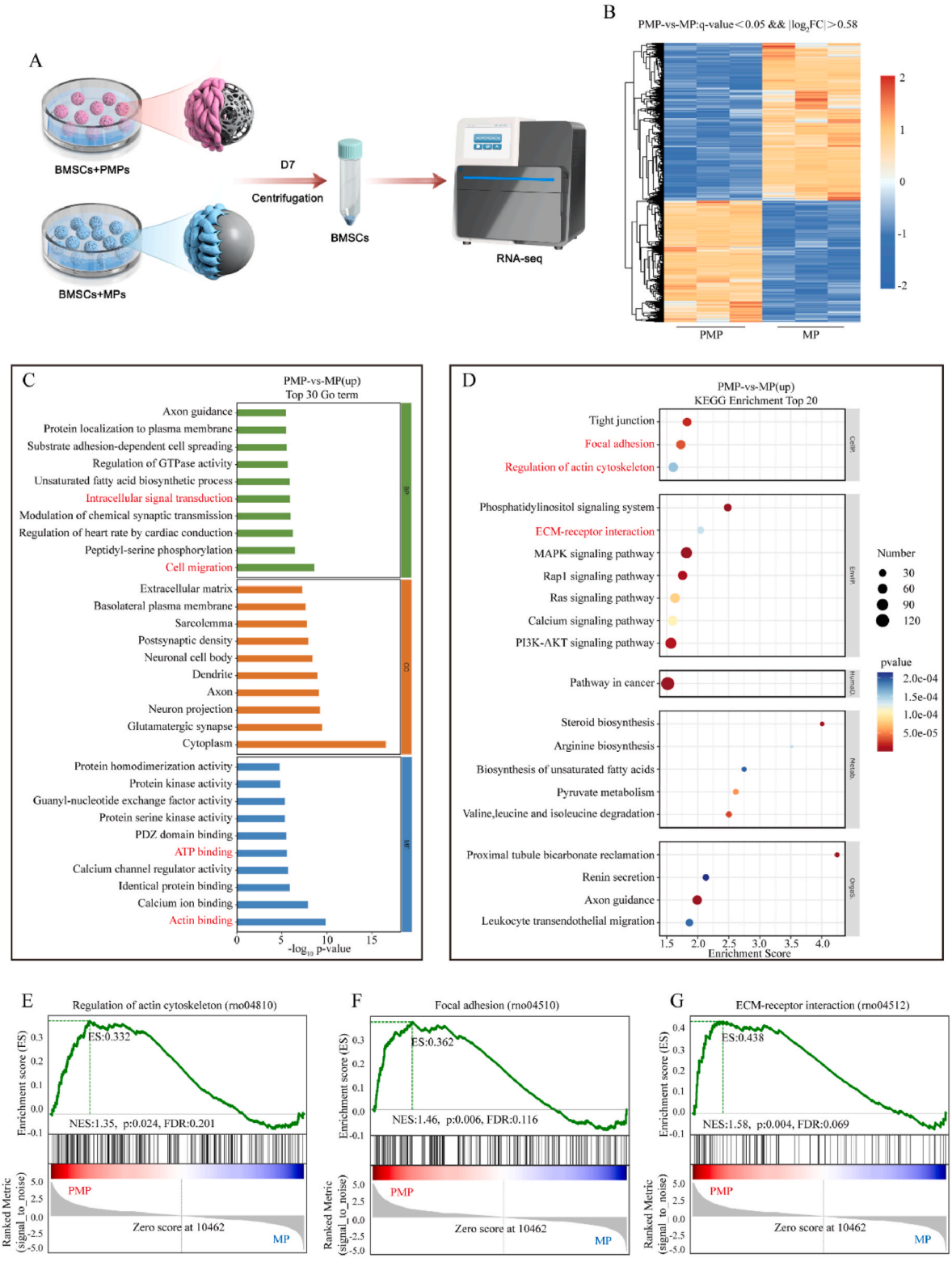


**Fig. 6.** RNA-seq reveals extensive transcriptomic changes in BMSCs under the influence of PMPs and MPs. A) Schematic diagram of the transcriptomic profile of BMSCs after one week of intervention with PMPs or MPs (n = 3); B) Heatmap of gene expression levels after cluster analysis ($p < 0.05$); C) GO enrichment analysis of differentially expressed genes between groups; D) KEGG enrichment analysis of differentially expressed genes between groups; E-G) GSEA analysis of Regulation of actin cytoskeleton, Focal adhesion, and ECM-receptor interaction signaling pathways.

mitochondrial fusion in BMSCs, thereby enhancing their functionality and promoting ATP production. Through Western blot analysis, we further observed elevated expression levels of the mitochondrial fusion-related proteins (MFN1 and MFN2) and the fission-related protein (DRP1) in the PMP group (Fig. 5N and O). These findings indicate that PMP stimulates a more vigorous mitochondrial dynamic process in BMSCs, which is essential for maintaining mitochondrial homeostasis. Specifically, the upregulation of MFN1 and MFN2 facilitates the formation of fusion mitochondria with heightened metabolic activity, while damaged or dysfunctional mitochondria are eliminated through DRP1-mediated mitochondrial division [21]. In summary, PMPs stimulated BMSCs to upregulate the expression of proteins related to glucose metabolism and mitochondrial dynamics, thereby promoting the production of ATP. This process provided robust support for BMSCs to play various biological functions.

### 3.3. Transcriptomic differences among BMSCs under the influence of MPs and PMPs

RNA-seq is an innovative high-throughput sequencing technology that enables comprehensive observation of cellular transcriptome changes from a global perspective [50]. Consequently, this chapter employs this methodology to juxtapose cellular responses to PMPs and MPs at the transcriptional level, aiming to elucidate the molecular mechanisms underpinning the aforementioned alterations in cellular functionality. After culturing BMSCs with PMPs or MPs for 7 days, RNA-seq was used to detect the samples (Fig. 6A). The principal component analysis (PCA) showed good reproducibility among samples from each group (Fig. S6). Each group of samples was independently repeated three times, and the expression level of each gene was standardized by calculating the number of fragments per kilobase of transcript per million reads (FPKM). We performed a comparison between PMP and MP groups to identify differentially expressed genes (DEGs) in BMSCs. The heatmap of all DEGs exhibited the changes in the transcriptome profile of BMSCs among the groups (Fig. 6B). Specifically, in comparison to the MP group, 3432 genes exhibited upregulation and 2639 genes showed downregulation in the PMP group (Fig. S7). This indicated that the topological variances among the microparticles have a substantial and distinguishable influence on BMSCs. We further conducted Gene Ontology (GO) enrichment analysis on the upregulated DEGs (PMP vs. MP) and found that several key GO terms were significantly enriched in the PMP group, including intracellular signal transduction, cell migration, ATP binding, and actin binding (Fig. 6C). We classified the differentially expressed genes in these items and drew a heat map (Fig. S8). We found that a large number of genes involved in cell adhesion and cytoskeletal remodeling and contraction were among the top 15 upregulated genes in these items. This indicates that significant mechanical remodeling occurred in BMSCs under the influence of PMPs. Further, kyoto encyclopedia of genes and genomes (KEGG) enrichment analysis was performed to determine the activated signaling pathways of PMPs on BMSCs. We found that signaling pathways related to cell mechanics were significantly enhanced, including focal adhesions, regulation of actin cytoskeleton, and extracellular matrix receptors (Fig. 6D–G). Notably, these signaling pathways are not independent; instead, they are interrelated and collaborate to promote the transmission of mechanical signals in the cellular environment. Focal adhesions (FAs) are complex multi-protein structures formed by the activation of integrin-β1, acting as mechanosensors to sense mechanical signals in the microenvironment and transduce them across the membrane by regulating the actin cytoskeleton. The actin cytoskeleton is crucial for converting mechanical signals into biochemical signals and promoting nuclear entry [51,52]. On one hand, the synthesis of the actin cytoskeleton can inhibit the core function of Hippo kinase, thereby protecting YAP protein from degradation [53]; on the other hand, cytoskeletal contraction can transmit mechanical signals to the nucleus through the nuclear-cytoskeletal linker (LINC) complex, promoting nuclear pore opening and assisting in the nuclear translocation of YAP protein, thereby triggering changes in cell function [20,54–56]. However, we also found that the MAPK pathway and PI3K/AKT pathway were highly enriched. Previous studies have shown that these two pathways are closely related to cell processes such as proliferation, differentiation, and metabolism of BMSCs [57,58]. Therefore, we compared the activation levels of these three pathways through WB experiments. The results indicated that the activation of YAP was the most significant compared to the MAPK pathway and PI3K/AKT pathway (Fig. S9). Therefore, we hypothesized that PMPs enhance the activation of the FA signaling pathway in BMSCs by increasing the expression of integrin-β1. This upregulation leads to the synthesis and contraction of the cytoskeleton, thereby inhibiting the degradation of YAP and promoting its nuclear translocation. Thus, these events initiate functional changes in BMSCs (Fig. 1).

### 3.4. PMPs activate the FA signaling pathway in BMSCs to inhibit the degradation of YAP and promote its nuclear translocation

To validate above hypothesis, we initially conducted immunofluorescence staining to evaluate the expression of integrin-β1 and vinculin. The results demonstrated a higher fluorescence intensity of integrin-β1 and vinculin in the PMP group, with notable presentation of highly clustered dot-like morphology in the vinculin, indicative of FAs maturation [59]; however, such characteristics were absent in the MP group (Fig. 7A–C). These findings suggest that the topological cues of PMPs promoted the expression of integrin-β1 and vinculin, thereby accelerating FA formation and maturation. Subsequently, we conducted a comparison of nuclear pore size between the two groups. Using TEM, we observed that the average diameter of nuclear pores in the PMP group was 1.26 times larger than that in the MP group (Fig. 7E and S10), which indicating that PMPs may facilitate the entry of YAP protein into the cell nucleus. This was further confirmed by immunofluorescence staining where YAP fluorescence was stronger and co-localized with DAPI in the PMP group, while it appeared fainter and dispersed within cytoplasm in MP group (Fig. 7A and D). Finally, to demonstrate that the mechanical reorganization of cells and the nuclear translocation of YAP in the PMP group are directly induced by activation of the activation of FA signaling pathway, we introduced the PMP + RGD group (an integrin receptor inhibitor) [39] and the MP + pyintegrin group (an integrin receptor agonist) [60,61] in our experiment, and compared alterations in relevant protein expression using WB technology (Fig. 7F–K). Focal adhesion kinase (FAK) is a crucial constituent of focal adhesions; its phosphorylation activation (pFAK) promotes G-actin polymerization into F-actin and stimulates myosin light chain phosphorylation (pMLC), resulting in cytoskeletal contraction [59,62]. Our WB band comparison analysis revealed higher levels of pFAK and pMLC expression in the PMP group compared to the MP group, while G-actin expression was lower. Following pyintegrin intervention in MP cells, protein expression reversed to reach similar levels as observed in the PMP group. Additionally, partial inhibition of integrin-β1 through RGD treatment significantly reduced pFAK and pMLC expression while increasing free G-actin levels within the PMP group. The abundance of YAP protein within cells is regulated by its phosphorylation degradation process; thus, calculating YAP/pYAP ratio provides an intuitive reflection of YAP activity within cells. Lamin A/C is a mechanosensitive protein located within the nuclear membrane whose expression correlates with nuclear membrane tension and permeability reactivity. Our WB results indicate that for YAP/pYAP and Lamin AC expressions: PMP ≈ MP + pyintegrin > MP ≈ PMP + RGD. Based on these findings, we conclude that cell mechanical remodeling and nuclear translocation of YAP within the PMP group were triggered by activation of the FA signaling pathway.

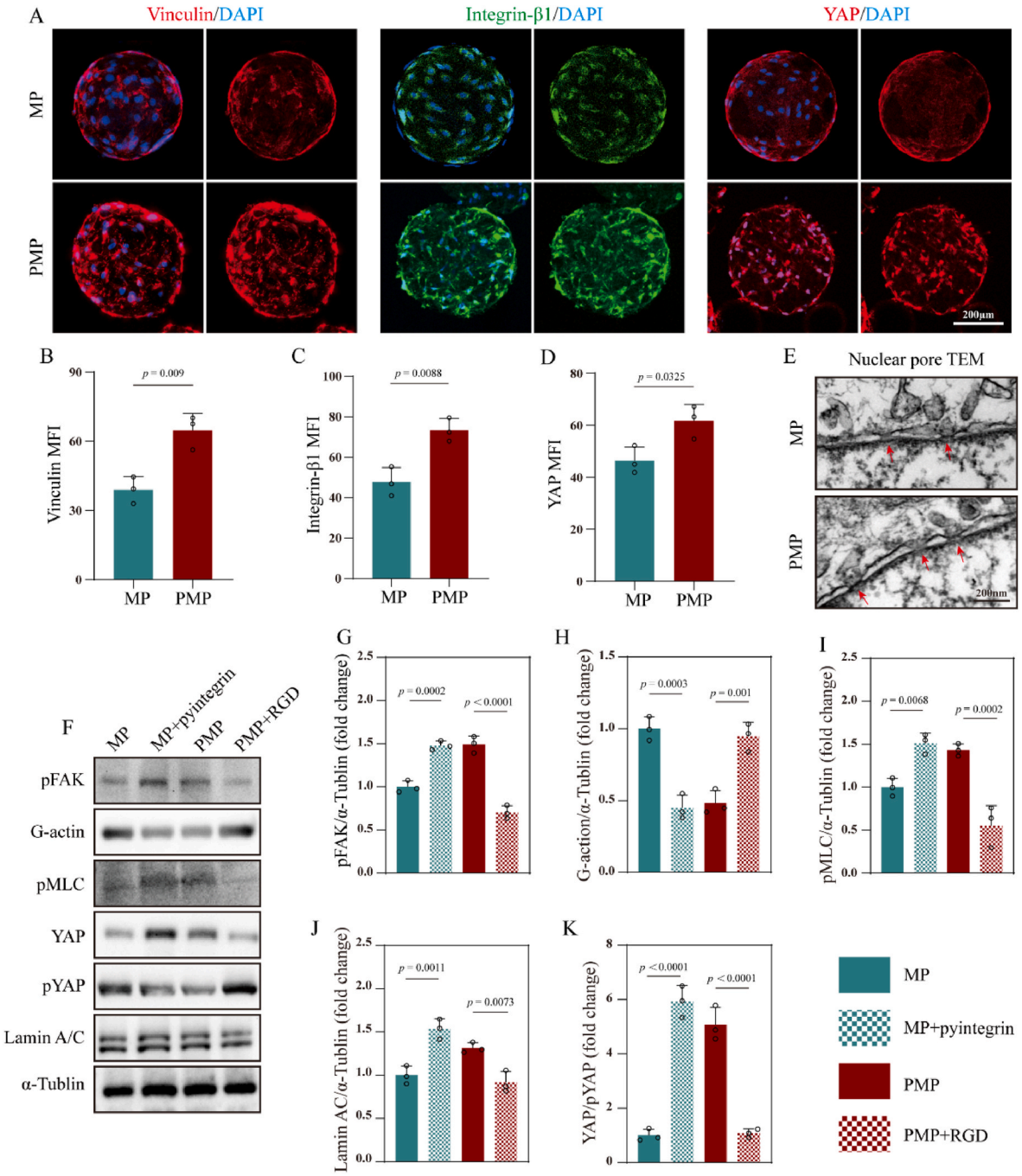


**Fig. 7.** The differences of FA signaling pathway on mechanotransduction in BMSCs under the influence of PMPs or MPs. A-D) Representative images and semi-quantitative analysis of immunofluorescence staining for Integrin-β1, Vinculin, and YAP in BMSCs within PMPs and MPs; E) Representative TEM images of nuclear pore morphology in different groups; F-J) Representative Western blot bands and quantitative analysis of mechano-related proteins in BMSCs within PMPs and MPs groups under the activation or inhibition of integrin-β1 (n = 3).

### *3.5. The nuclear translocation of YAP protein results in the enhancement of the function of BMSCs in the PMP group*

In order to investigate the impact of increased YAP abundance and nuclear translocation on cellular function, we conducted corresponding suppression and rescue experiments. Specifically, we augmented the PMP + Verteporfin group (a YAP inhibitor) [63] and the MP + PY60 group (a YAP agonist) [64] in our study, and compared differences in cell proliferation, osteogenesis, paracrine effects, and metabolism among these groups. Flow cytometry analysis of Ki67 cells revealed that drug-induced inhibition/activation of YAP significantly reduced the disparity in Ki67-positive cell ratio between the MP and PMP groups (Fig. 8A and S11). Furthermore, PY60 treatment notably enhanced OPN and RUNX2 expression in the MP group during osteogenic differentiation, while Verteporfin treatment led to a significant reduction in protein expression within the PMP group (Fig. 8B–D). Subsequent detection of TGF-β and VEGFA exhibited a similar trend with supernatant concentration ranking as follows: PMP ≈ MP + PY60 > MP ≈ PMP + Verteporfin (Fig. S12). Lastly, examination of mitochondrial dynamic-related proteins and glucose metabolism-related proteins across each group indicated that any protein expression advantage of PMP over MP was eliminated by PY60/Verteporfin treatment

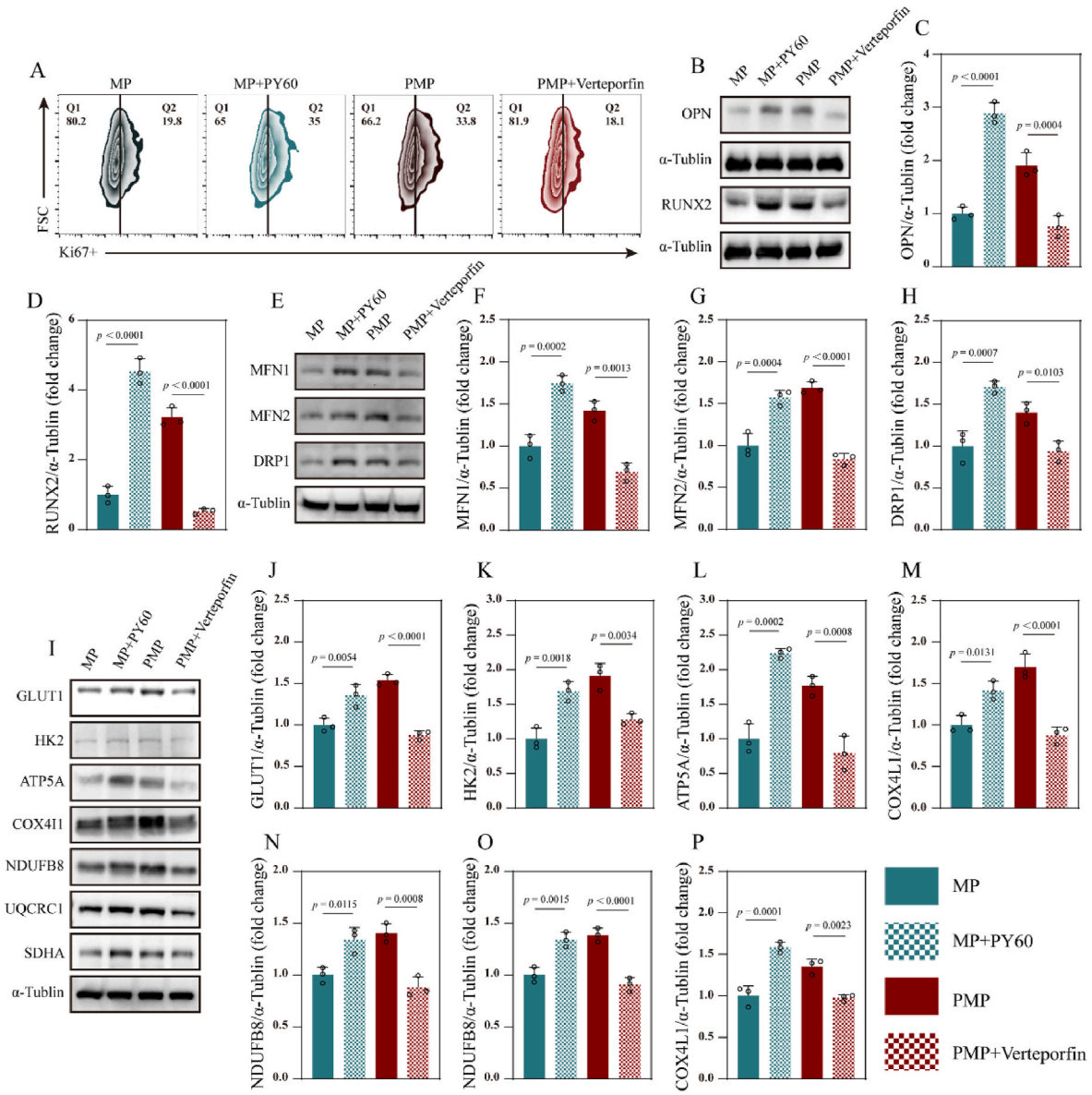


**Fig. 8.** Verification of the impact of YAP on BMSCs' functions. A) Flow cytometry detection of the proportion of Ki-67 positive cells in PMPs and MPs groups under the activation or inhibition of YAP; B-D) Representative Western blot bands and statistical analysis of osteogenic-related proteins in BMSCs from various groups under the activation or inhibition of YAP (n = 3).

(Fig. 8E–P). Overall, these findings suggest that the activation and nuclear translocation of YAP are primary drivers for divergent cellular functions observed between the PMP and MP groups.

### 3.6. *In vivo experiment*

As illustrated in Fig. 9A, a rat femoral condyle defect model was established, and BMSC-seeded PMPs and MPs were employed to evaluate the effect of BMSCs interacting with PMPs or MPs on bone healing in vivo. During the modeling procedure, we observed that the bone tissue, periosteum, and muscle tissue surrounding the defect area formed an effective barrier, which confined the microparticle scaffold to the defect site. Additionally, we found that when the microparticle scaffold was mixed with blood, an annealing fixation phenomenon occurred during the coagulation process, thereby enhancing its stability and local retention (Fig. S13). Consequently, we have determined that in the complex in vivo environment, the implanted microparticle scaffolds can stably reside in the target area and effectively exert their reparative functions.

The resolution of inflammation in the damaged area was analyzed by conducting immunofluorescence staining for Arg-1 and iNOS at 2 and 4 weeks post-operation (Fig. 9B and C). As presented in Fig. 9D and E, the PMP group demonstrated the most potent anti-inflammatory capacity compared with the control group (untreated) and the MP group at all time points. Specifically, the PMP group exhibited the highest fluorescence intensity of Arg-1 and the weakest fluorescence intensity of iNOS. Angiogenesis in each group was examined by using CD31 fluorescent staining to mark the new blood vessels in the sections, and it was found that there were more CD31-positive regions in the PMP group at both 2 and 4 weeks (Fig. 9B and F). Based on these outcomes, it is believed that PMP-treated BMSCs possess a stronger paracrine function, shaping the local microenvironment conducive to bone tissue repair through angiogenesis and inflammation regulation.

Subsequently, bone repair was inspected at the microscopic scale under the assistance of Micro-CT. As shown in Fig. 10A, only a small quantity of newly formed bone tissue was present in the defect area of the Control group at 2 and 4 weeks, indicating that the femoral condyle defect we established was of a critical size exceeding the capacity for

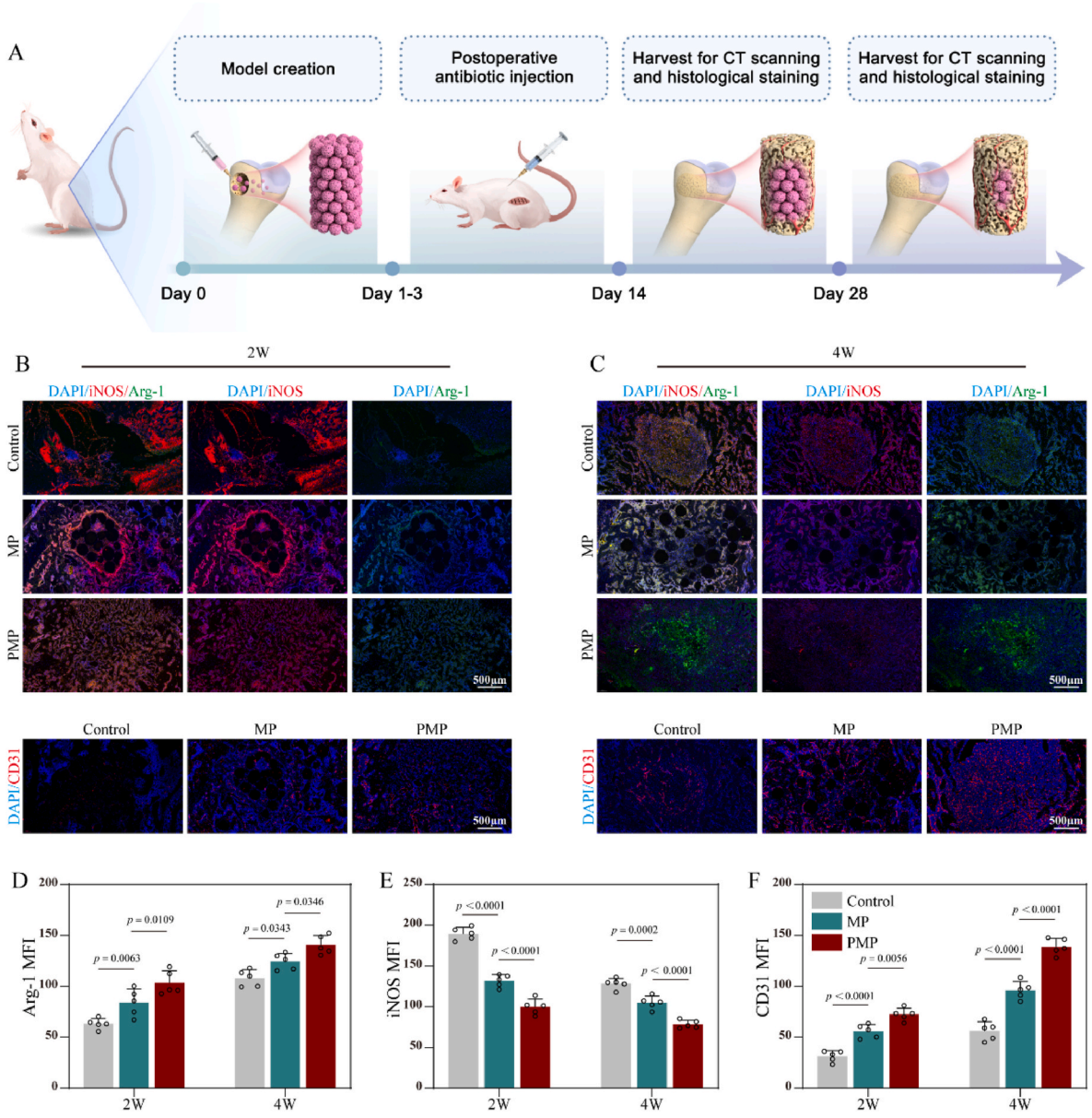


**Fig. 9.** PMPs or MPs triggers paracrine signaling of BMSCs to promote the remodeling of the microenvironment in the bone defect area in vivo. A) Schematic diagram of the animal experiment process, delivering BMSCs into the femoral condyle defect model of rats using PMP or MP as a carrier; B-F) Representative immunofluorescence staining and related quantitative analysis of iNOS, Arg-1, and CD31 in each group at 2 and 4 weeks (n = 5).

spontaneous healing. Both the PMP group and the MP group facilitated bone formation to a certain extent in the defect area. However, a further comparison between the two groups revealed that the PMP group performed superiorly to the MP group. Furthermore, the bone microstructure parameters obtained from the CT scans were quantified, and the bone formation and morphological performance of the defect area were compared. It was found that at the same time point, the PMP group had the highest BMD, BV/TV, Tb.th, and the lowest Tb.sp (Fig. 10B–E). These results suggest that BMSCs under the influence of PMP have the strongest osteogenic capacity and efficiently promote the formation of new bone tissue. H&E staining and Masson's staining of each group were evaluated to obtain histological cues for bone repair. Fig. 10F shows a complete sagittal coronal section of the femur along with the corresponding enlarged image of the central region of the defect, where the newly formed bone tissue can be observed. Through comparison, it was discovered that the newly formed bone tissue in the Control group was mainly located at the edge of the defect area, while the newly formed bone tissue in the PMP group and the MP group was evenly distributed throughout the defect area. This implies that the BMSCs delivered by the microparticles further differentiated and matured in vivo to form new bone centers. We further compared the H&E and Masson's staining of the material implantation group under high-power microscopic fields. As shown in Fig. S14, the MPs are indicated by the green arrows, and the PMPs are indicated by the red arrows. It can be distinctly observed that both the PMPs and MPs exhibited well-preserved morphologies after 2 and 4 weeks of implantation. Notably, compared with the MP group, the PMP group exhibited significantly more new bone tissue formation both within and surrounding the PMPs, as well as a tighter integration between the PMPs and the newly formed bone tissue. Therefore, it is believed that PMP not only potentiates the osteogenic differentiation of BMSCs, resulting in the establishment of new bone calcification centers, but also enhances the efficacious integration of itself with the surrounding bone tissue. Finally, immunofluorescence staining for OPN and OCN was carried out to observe the osteoblast status in each group (Fig. 10G and I). The result revealed that the fluorescence intensity of the two conformed to the pattern of PMP > MP > Control group

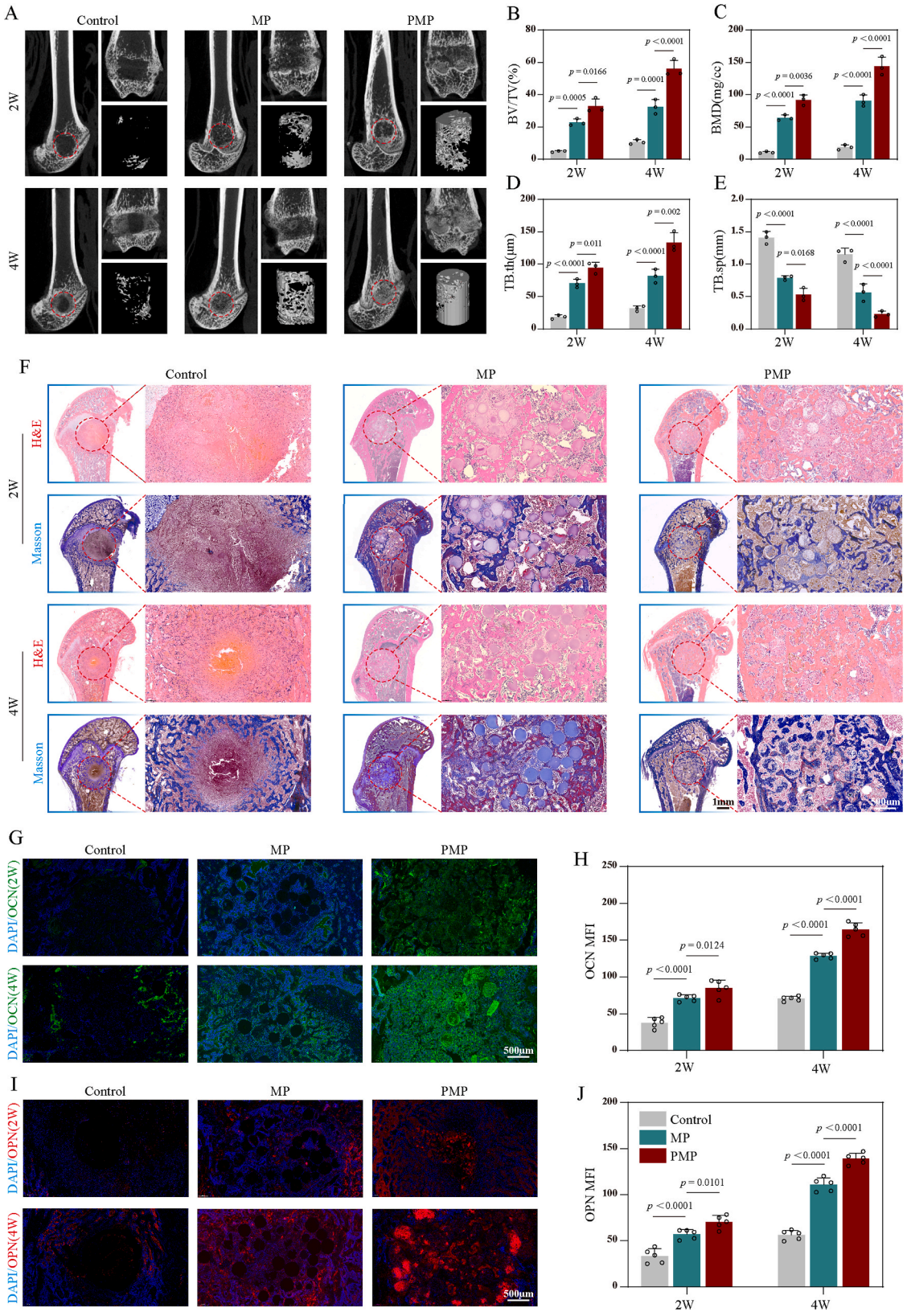


**Fig. 10.** PMPs and MPs as carriers deliver BMSCs to promote bone tissue regeneration in the defect area. A) Representative Micro-CT three-dimensional reconstruction images of femoral condyle samples from each group at 2 and 4 weeks; B-E) Quantitative analysis of BV/TV, BMD, Tb.Th, and Tb.Sp in the bone defect area of each group (n = 5); F) Representative images of HE and Masson staining for each group at 2 and 4 weeks; G, H) Representative images of OCN immunofluorescence staining and related semi-quantitative analysis for each group at 2 and 4 weeks (n = 5); I, J) Representative images of OPN immunofluorescence staining and related semi-quantitative analysis for each group at 2 and 4 weeks (n = 5).

(Fig. 10H and J). It is postulated that this phenomenon is conducive from two aspects: the direct pro-osteogenic impact of PMP on BMSCs, and the enhanced functionality of BMSCs under the influence of PMP expedites local microenvironment remodeling, facilitating bone tissue repair.

## 4. Conclusion

In summary, we investigated the influence of topological differences between PMPs and MPs on the functions of BMSCs. We discovered that the porous structure of PMPs could be sensed by FAs and affect the degradation and nuclear translocation of YAP protein through the synthesis and contraction of F-actin. Specifically, PMPs activated FAs to promote the polymerization of G-actin into F-actin, thereby inhibiting the phosphorylation and degradation of YAP protein in the cytoplasm. Meanwhile, FAs promoted the phosphorylation of myosin to induce contraction of F-actin, which increased the tension of the nucleus, stretched nuclear pores and enhanced the nuclear translocation of YAP. As a result, BMSCs exhibited stronger proliferation, osteogenic, and paracrine activities, which play important roles in the process of bone regeneration. At the same time, the glucose metabolism capacity of BMSCs was significantly enhanced, providing strong energy support for the active cellular behavior. We believe that this study reveals the powerful potential of the topological features of PMPs to regulate cell function through mechanical signaling pathways, which can provide valuable insights for the design of BTE scaffolds based on microparticle systems. We also acknowledge that this study has certain limitations, that we did not further investigate the effect of the pore size of PMPs on the mechanical conduction process. However, we will conduct further research on this issue in our subsequent studies.

## CRediT authorship contribution statement

**Jiannan Mao:** Writing – original draft, Software, Methodology, Investigation, Funding acquisition, Formal analysis, Conceptualization. **Yichang Xu:** Visualization, Resources, Methodology, Investigation, Data curation. **Wenbo Wang:** Validation, Supervision, Software, Methodology, Formal analysis. **Xiongwei Deng:** Visualization, Validation, Software, Investigation. **Yujian Hui:** Methodology, Investigation. **Min Rui:** Validation, Supervision, Software. **Jincheng Tang:** Methodology, Funding acquisition. **Wei Wang:** Supervision, Methodology, Investigation. **Yiyang Huang:** Validation, Investigation, Formal analysis. **Liang Wu:** Software, Methodology. **Kun Xi:** Writing – review & editing, Writing – original draft, Resources, Project administration, Investigation, Funding acquisition, Conceptualization. **Yunrong Zhu:** Writing – original draft, Visualization, Project administration, Investigation, Data curation. **Yong Gu:** Writing – review & editing, Writing – original draft, Investigation, Funding acquisition, Conceptualization. **Liang Chen:** Writing – review & editing, Writing – original draft, Resources, Project administration, Investigation, Funding acquisition, Conceptualization.

## Data statement

All the data supporting the conclusions are present in the manuscript, along with the supplementary information. Additional data related to this paper may be requested from the corresponding author upon reasonable request.

## Ethics approval and consent to participate

This study was approved by the Ethics Committee of Soochow University (Approval No. SUDA20240102A01) and good surgical and therapeutic outcomes were achieved.

## Declaration of competing interest

The authors declare that they have no known competing financial interests or personal relationships that could have appeared to influence the work reported in this paper.

## Acknowledgment

This work was supported by the National Natural Science Foundation of China (82120108017, 82072438, 82272501, 82102589, 82302683), Social Development Project of Jiangsu Province (BE2021646), Project 333 of Jiangsu Province(2069999); the Natural Science Foundation of Jiangsu Province (BK20211504, BK20230215), Suzhou Gusu Health Talent Program (GSWS2020001, GSWS2021009, GSWS2021007), Jiangsu Innovative and Entrepreneurial Talent Program (JSSCBS20211570), Medical Health Science and Technology Innovation Program of Suzhou (SKY2022119), Soochow University Medical + X project (ML12202923), Major Scientific Research Program of Wuxi Municipal Health Commission (Z202008, Z202313).

## Appendix A. Supplementary data

Supplementary data to this article can be found online at https://doi.org/10.1016/j.bioactmat.2025.02.032.

## References

[1] E.H. Schemitsch, Size matters: defining critical in bone defect size, J. Orthop. Trauma 31 (Suppl 5) (2017) S20–S22, https://doi.org/10.1097/BOT.0000000000000978.
[2] R.T. Annamalai, X. Hong, N.G. Schott, G. Tiruchinapally, B. Levi, J.P. Stegemann, Injectable osteogenic microtissues containing mesenchymal stromal cells conformally fill and repair critical-size defects, Biomaterials 208 (2019) 32–44, https://doi.org/10.1016/j.biomaterials.2019.04.001.
[3] E. Roddy, M.R. DeBaun, A. Daoud-Gray, Y.P. Yang, M.J. Gardner, Treatment of critical-sized bone defects: clinical and tissue engineering perspectives, Eur. J. Orthop. Surg. Traumatol. 28 (3) (2018) 351–362, https://doi.org/10.1007/s00590-017-2063-0.
[4] J. Song, L. Li, L. Fang, E. Zhang, Y. Zhang, Z. Zhang, P. Vangari, Y. Huang, F. Tian, Advanced strategies of scaffolds design for bone regeneration, BMEMat 1 (4) (2023) e12046, https://doi.org/10.1002/bmm2.12046.
[5] J. Wang, M. Liu, C. Yang, Y. Pan, S. Ji, N. Han, G. Sun, Biomaterials for bone defect repair: types, mechanisms and effects, Int. J. Artif. Organs 47 (2) (2024) 75–84, https://doi.org/10.1177/03913988231218884.
[6] S. Chen, X. Chen, Z. Geng, J. Su, The horizon of bone organoid: a perspective on construction and application, Bioact. Mater. 18 (2022) 15–25, https://doi.org/10.1016/j.bioactmat.2022.01.048.
[7] A.S. Caldwell, B.A. Aguado, K.S. Anseth, Designing microgels for cell culture and controlled assembly of tissue microenvironments, Adv. Funct. Mater. 30 (37) (2020), https://doi.org/10.1002/adfm.201907670.
[8] F. Zheng, R. Tian, H. Lu, X. Liang, M. Shafiq, S. Uchida, H. Chen, M. Ma, Droplet microfluidics powered hydrogel microparticles for stem cell-mediated biomedical applications, Small 20 (42) (2024) e2401400, https://doi.org/10.1002/smll.202401400.
[9] A.C. Daly, L. Riley, T. Segura, J.A. Burdick, Hydrogel microparticles for biomedical applications, Nat. Rev. Mater. 5 (1) (2020) 20–43, https://doi.org/10.1038/s41578-019-0148-6.
[10] C. Bektas, Y. Mao, Hydrogel microparticles for bone regeneration, Gels 10 (1) (2023), https://doi.org/10.3390/gels10010028.
[11] A. Bettini, P. Camelliti, D.J. Stuckey, R.M. Day, Injectable biodegradable microcarriers for iPSC expansion and cardiomyocyte differentiation, Adv. Sci. 11 (32) (2024) e2404355, https://doi.org/10.1002/advs.202404355.
[12] S.L. Ding, X. Liu, X.Y. Zhao, K.T. Wang, W. Xiong, Z.L. Gao, C.Y. Sun, M.X. Jia, C. Li, Q. Gu, M.Z. Zhang, Microcarriers in application for cartilage tissue engineering: recent progress and challenges, Bioact. Mater. 17 (2022) 81–108, https://doi.org/10.1016/j.bioactmat.2022.01.033.
[13] S.S. Datta, A. Abbaspourrad, E. Amstad, J. Fan, S.H. Kim, M. Romanowsky, H. C. Shum, B. Sun, A.S. Utada, M. Windbergs, S. Zhou, D.A. Weitz, 25th anniversary article: double emulsion templated solid microcapsules: mechanics and controlled release, Adv. Mater. 26 (14) (2014) 2205–2218, https://doi.org/10.1002/adma.201305119.
[14] S. Ma, N. Mukherjee, E. Mikhailova, H. Bayley, Gel microrods for 3D tissue printing, Adv. Biosyst. 1 (8) (2017) e1700075, https://doi.org/10.1002/adbi.201700075.
[15] M. Ermis, E. Antmen, V. Hasirci, Micro and Nanofabrication methods to control cell-substrate interactions and cell behavior: a review from the tissue engineering perspective, Bioact. Mater. 3 (3) (2018) 355–369, https://doi.org/10.1016/j.bioactmat.2018.05.005.

[16] A.T. Nguyen, S.R. Sathe, E.K. Yim, From nano to micro: topographical scale and its impact on cell adhesion, morphology and contact guidance, J. Phys. Condens. Matter 28 (18) (2016) 183001, https://doi.org/10.1088/0953-8984/28/18/183001.
[17] S. Nemec, Kajnrm. Kilian, Materials control of the epigenetics underlying cell plasticity, Nat. Rev. Mater. 6 (1) (2021) 69–83, https://doi.org/10.1038/s41578-020-00238-z.
[18] X. Wang, V. Agrawal, C.L. Dunton, Y. Liu, R.K.A. Virk, P.A. Patel, L. Carter, E. M. Pujadas, Y. Li, S. Jain, H. Wang, N. Ni, H.M. Tsai, N. Rivera-Bolanos, J. Frederick, E. Roth, R. Bleher, C. Duan, P. Ntziachristos, T.C. He, R.R. Reid, B. Jiang, H. Subramanian, V. Backman, G.A. Ameer, Chromatin reprogramming and bone regeneration in vitro and in vivo via the microtopography-induced constriction of cell nuclei, Nat. Biomed. Eng. 7 (11) (2023) 1514–1529, https://doi.org/10.1038/s41551-023-01053-x.
[19] T.L. Downing, J. Soto, C. Morez, T. Houssin, A. Fritz, F. Yuan, J. Chu, S. Patel, D. V. Schaffer, S. Li, Biophysical regulation of epigenetic state and cell reprogramming, Nat. Mater. 12 (12) (2013) 1154–1162, https://doi.org/10.1038/nmat3777.
[20] Y. Li, Z. Zhong, C. Xu, X. Wu, J. Li, W. Tao, J. Wang, Y. Du, S. Zhang, 3D micropattern force triggers YAP nuclear entry by transport across nuclear pores and modulates stem cells paracrine, Natl. Sci. Rev. 10 (8) (2023) nwad165, https://doi.org/10.1093/nsr/nwad165.
[21] J. Na, Z. Yang, Q. Shi, C. Li, Y. Liu, Y. Song, X. Li, L. Zheng, Y. Fan, Extracellular matrix stiffness as an energy metabolism regulator drives osteogenic differentiation in mesenchymal stem cells, Bioact. Mater. 35 (2024) 549–563, https://doi.org/10.1016/j.bioactmat.2024.02.003.
[22] Z. Cai, H. Jiang, T. Lin, C. Wang, J. Ma, R. Gao, Y. Jiang, X.J.M.T.A. Zhou, Microspheres in bone regeneration: fabrication, properties and applications, Mater. Today Adv. 16 (2022) 100315, https://doi.org/10.1016/j.mtadv.2022.100315.
[23] J. Lin, S. Jia, F. Cao, J. Huang, J. Chen, J. Wang, P. Liu, H. Zeng, X. Zhang, W.J.A.F. M. Cui, Research progress on injectable microspheres as new strategies for the treatment of osteoarthritis through promotion of cartilage repair, Adv. Funct. Mater. 30 (37) (2024) 2400585, https://doi.org/10.1002/adfm.202400585.
[24] W. Tang, N.G. Fischer, X. Kong, T. Sang, Z.J.B. Ye, Hybrid coatings on dental and orthopedic titanium implants: current advances and challenges, BMEMat (2024) e12105, https://doi.org/10.1002/bmm2.12105.
[25] P. Roach, D. Eglin, K. Rohde, C.C. Perry, Modern biomaterials: a review - bulk properties and implications of surface modifications, J. Mater. Sci. Mater. Med. 18 (7) (2007) 1263–1277, https://doi.org/10.1007/s10856-006-0064-3.
[26] M. Rahmati, M.J.M.T.C. Mozafari, Protein adsorption on polymers, Mater. Today Commun. 17 (2018) 527–540, https://doi.org/10.1016/j.mtcomm.2018.10.024.
[27] M.M. Martino, F. Tortelli, M. Mochizuki, S. Traub, D. Ben-David, G.A. Kuhn, R. Müller, E. Livne, S.A. Eming, J.A. Hubbell, Engineering the growth factor microenvironment with fibronectin domains to promote wound and bone tissue healing, Sci. Transl. Med. 3 (100) (2011), https://doi.org/10.1126/scitranslmed.3002614, 100ra89.
[28] A. Arthur, S. Gronthos, Clinical application of bone marrow mesenchymal stem/stromal cells to repair skeletal tissue, Int. J. Mol. Sci. 21 (24) (2020), https://doi.org/10.3390/ijms21249759.
[29] J. Wang, Z. Chen, M. Sun, H. Xu, Y. Gao, J. Liu, M. Li, Characterization and therapeutic applications of mesenchymal stem cells for regenerative medicine, Tissue Cell 64 (2020) 101330, https://doi.org/10.1016/j.tice.2020.101330.
[30] Y. Jiang, P. Zhang, X. Zhang, L. Lv, Y. Zhou, Advances in mesenchymal stem cell transplantation for the treatment of osteoporosis, Cell Prolif. 54 (1) (2021) e12956.
[31] X. Fu, G. Liu, A. Halim, Y. Ju, Q. Luo, A.G. Song, Mesenchymal stem cell migration and tissue repair, Cells 8 (8) (2019), https://doi.org/10.3390/cells8080784.
[32] C. Liu, K. Xiao, L. Xie, Advances in the regulation of macrophage polarization by mesenchymal stem cells and implications for ALI/ARDS treatment, Front. Immunol. 13 (2022) 928134, https://doi.org/10.3389/fimmu.2022.928134.
[33] J.Y. Ding, M.J. Chen, L.F. Wu, G.F. Shu, S.J. Fang, Z.Y. Li, X.R. Chu, X.K. Li, Z. G. Wang, J.S. Ji, Mesenchymal stem cell-derived extracellular vesicles in skin wound healing: roles, opportunities and challenges, Mil Med Res 10 (1) (2023) 36, https://doi.org/10.1186/s40779-023-00472-w.
[34] T. Scholzen, J. Gerdes, The Ki-67 protein: from the known and the unknown, J. Cell. Physiol. 182 (3) (2000) 311–322, https://doi.org/10.1002/(SICI)1097-4652(200003)182:3<311::AID-JCP1>3.0.CO;2-9.
[35] S. Vimalraj, Alkaline phosphatase: structure, expression and its function in bone mineralization, Gene 754 (2020) 144855, https://doi.org/10.1016/j.gene.2020.144855.
[36] L. Yu, M. Wei, Biomineralization of collagen-based materials for hard tissue repair, Int. J. Mol. Sci. 22 (2) (2021), https://doi.org/10.3390/ijms22020944.
[37] A. Salhotra, H.N. Shah, B. Levi, M.T. Longaker, Mechanisms of bone development and repair, Nat. Rev. Mol. Cell Biol. 21 (11) (2020) 696–711, https://doi.org/10.1038/s41580-020-00279-w.
[38] J. Pajarinen, T. Lin, E. Gibon, Y. Kohno, M. Maruyama, K. Nathan, L. Lu, Z. Yao, S. B. Goodman, Mesenchymal stem cell-macrophage crosstalk and bone healing, Biomaterials 196 (2019) 80–89, https://doi.org/10.1016/j.biomaterials.2017.12.025.
[39] Y. Zhang, R. Sheng, J. Chen, H. Wang, Y. Zhu, Z. Cao, X. Zhao, Z. Wang, C. Liu, Z. Chen, P. Zhang, B. Kuang, H. Zheng, C. Shen, Q. Yao, W. Zhang, Silk fibroin and sericin differentially potentiate the paracrine and regenerative functions of stem cells through multiomics analysis, Adv. Mater. 35 (20) (2023) e2210517, https://doi.org/10.1002/adma.202210517.
[40] M.Y. Noh, S.M. Lim, K.W. Oh, K.A. Cho, J. Park, K.S. Kim, S.J. Lee, M.S. Kwon, S. H. Kim, Mesenchymal stem cells modulate the functional properties of microglia via TGF-β secretion, Stem. Cells Transl. Med. 5 (11) (2016) 1538–1549, https://doi.org/10.5966/sctm.2015-0217.
[41] F. Liu, H. Qiu, M. Xue, S. Zhang, X. Zhang, J. Xu, J. Chen, Y. Yang, J. Xie, MSC-secreted TGF-β regulates lipopolysaccharide-stimulated macrophage M2-like polarization via the Akt/FoxO1 pathway, Stem Cell Res. Ther. 10 (1) (2019) 345, https://doi.org/10.1186/s13287-019-1447-y.
[42] H. Zhang, M. Zhang, D. Zhai, C. Qin, Y. Wang, J. Ma, H. Zhuang, Z. Shi, L. Wang, C. Wu, Polyhedron-like biomaterials for innervated and vascularized bone regeneration, Adv. Mater. 35 (42) (2023) e2302716, https://doi.org/10.1002/adma.202302716.
[43] S. Saberianpour, M. Heidarzadeh, M.H. Geranmayeh, H. Hosseinkhani, R. Rahbarghazi, M. Nouri, Tissue engineering strategies for the induction of angiogenesis using biomaterials, J. Biol. Eng. 12 (2018) 36, https://doi.org/10.1186/s13036-018-0133-4.
[44] L. Mao, L. Xia, J. Chang, J. Liu, L. Jiang, C. Wu, B. Fang, The synergistic effects of Sr and Si bioactive ions on osteogenesis, osteoclastogenesis and angiogenesis for osteoporotic bone regeneration, Acta Biomater. 61 (2017) 217–232, https://doi.org/10.1016/j.actbio.2017.08.015.
[45] P. Nowak-Sliwinska, K. Alitalo, E. Allen, A. Anisimov, A.W. Griffioen, Consensus guidelines for the use and interpretation of angiogenesis assays, Angiogenesis 21 (3) (2018) 425–532, https://doi.org/10.1007/s10456-018-9613-x.
[46] M. Rodrigues, N. Kosaric, C.A. Bonham, G.C. Gurtner, Wound healing: a cellular perspective, Physiol. Rev. 99 (1) (2019) 665–706, https://doi.org/10.1152/physrev.00067.2017.
[47] T.A. Wynn, K.M. Vannella, Macrophages in tissue repair, regeneration, and fibrosis, Immunity 44 (3) (2016) 450–462, https://doi.org/10.1016/j.immuni.2016.02.015.
[48] X. Jiang, W. Wang, J. Tang, M. Han, Y. Xu, L. Zhang, J. Wu, Y. Huang, Z. Ding, H. Sun, K. Xi, Y. Gu, L. Chen, Ligand-screened cerium-based MOF microcapsules promote nerve regeneration via mitochondrial energy supply, Adv. Sci. 11 (6) (2024) e2306780, https://doi.org/10.1002/advs.202306780.
[49] M. Giacomello, A. Pyakurel, C. Glytsou, L. Scorrano, The cell biology of mitochondrial membrane dynamics, Nat. Rev. Mol. Cell Biol. 21 (4) (2020) 204–224, https://doi.org/10.1038/s41580-020-0210-7.
[50] R. Hrdlickova, M. Toloue, B. Tian, RNA-Seq methods for transcriptome analysis, Wiley Interdiscip Rev. RNA 8 (1) (2017), https://doi.org/10.1002/wrna.1364.
[51] T. Panciera, L. Azzolin, M. Cordenonsi, S. Piccolo, Mechanobiology of YAP and TAZ in physiology and disease, Nat. Rev. Mol. Cell Biol. 18 (12) (2017) 758–770, https://doi.org/10.1038/nrm.2017.87.
[52] G. Halder, S. Dupont, S. Piccolo, Transduction of mechanical and cytoskeletal cues by YAP and TAZ, Nat. Rev. Mol. Cell Biol. 13 (9) (2012) 591–600, https://doi.org/10.1038/nrm3416.
[53] S. Ma, Z. Meng, R. Chen, K.L. Guan, The Hippo pathway: biology and pathophysiology, Annu. Rev. Biochem. 88 (2019) 577–604, https://doi.org/10.1146/annurev-biochem-013118-111829.
[54] Y. Kalukula, A.D. Stephens, J. Lammerding, S. Gabriele, Mechanics and functional consequences of nuclear deformations, Nat. Rev. Mol. Cell Biol. 23 (9) (2022) 583–602, https://doi.org/10.1038/s41580-022-00480-z.
[55] C.E. Zimmerli, M. Allegretti, V. Rantos, S.K. Goetz, A. Obarska-Kosinska, I. Zagoriy, A. Halavatyi, G. Hummer, J. Mahamid, J. Kosinski, M. Beck, Nuclear pores dilate and constrict in cellulo, Science 374 (6573) (2021) eabd9776, https://doi.org/10.1126/science.abd9776.
[56] S. Cho, J. Irianto, D.E. Discher, Mechanosensing by the nucleus: from pathways to scaling relationships, J. Cell Biol. 216 (2) (2017) 305–315, https://doi.org/10.1083/jcb.201610042.
[57] C. Wang, K. Lin, J. Chang, J. Sun, Osteogenesis and angiogenesis induced by porous β-CaSiO(3)/PDLGA composite scaffold via activation of AMPK/ERK1/2 and PI3K/Akt pathways, Biomaterials 34 (1) (2013) 64–77, https://doi.org/10.1016/j.biomaterials.2012.09.021.
[58] G.p. Dang, Y. Wei, Q.q. Wan, J.t. Gu, K.y. Wang, M.c. Wan, C.y. Wang, J.h. Song, Z. Mu, F.R.J.B. Tay, Regulatory mechanisms and regeneration strategies of the soft–hard tissue interface in the human periodontium, BMEMat (2024) e12069, https://doi.org/10.1002/bmm2.12069.
[59] S.J. Tan, A.C. Chang, S.M. Anderson, C.M. Miller, L.S. Prahl, D.J. Odde, A.R. Dunn, Regulation and dynamics of force transmission at individual cell-matrix adhesion bonds, Sci. Adv. 6 (20) (2020) eaax0317, https://doi.org/10.1126/sciadv.aax0317.
[60] B.S. Shah, M. Chen, T. Suzuki, M. Embree, K. Kong, C.H. Lee, L. He, L. Xiang, J. A. Ahn, S. Ding, J.J. Mao, Pyrintegrin induces soft tissue formation by transplanted or endogenous cells, Sci. Rep. 7 (2017) 36402, https://doi.org/10.1038/srep36402.
[61] H.W. Lee, S.Q. Khan, M.H. Faridi, C. Wei, N.J. Tardi, M.M. Altintas, H. A. Elshabrawy, S. Mangos, K.L. Quick, S. Sever, J. Reiser, V. Gupta, A podocyte-based automated screening assay identifies protective small molecules, J. Am. Soc. Nephrol. 26 (11) (2015) 2741–2752, https://doi.org/10.1681/ASN.2014090859.
[62] X. Xu, W. Wang, J. Zou, K. Kratz, Z. Deng, A. Lendlein, N. Ma, Histone modification of osteogenesis related genes triggered by substrate topography promotes human mesenchymal stem cell differentiation, ACS Appl. Mater. Interfaces 15 (25) (2023) 29752–29766, https://doi.org/10.1021/acsami.3c01481.
[63] C. Wei, C. You, L. Zhou, H. Liu, S. Zhou, X. Wang, R.J.C.E.J. Guo, Antimicrobial hydrogel microneedle loading verteporfin promotes skin regeneration by blocking mechanotransduction signaling, Chem. Eng. J. 472 (2023) 144866, https://doi.org/10.1016/j.cej.2023.144866.
[64] S.Z. Shalhout, P.Y. Yang, E.M. Grzelak, K. Nutsch, S. Shao, C. Zambaldo, J. Iaconelli, L. Ibrahim, C. Stanton, S.R. Chadwick, E. Chen, M. DeRan, S. Li, M. Hull, X. Wu, A.K. Chatterjee, W. Shen, F.D. Camargo, P.G. Schultz, M.J. Bollong,

YAP-dependent proliferation by a small molecule targeting annexin A2, Nat. Chem. Biol. 17 (7) (2021) 767–775, https://doi.org/10.1038/s41589-021-00755-0.